



Reservoir quality of Upper Cretaceous limestones (Ahlen-Fm., Beckum Member, Münsterland Cretaceous Basin): effects of cementation and compaction on the compactable depositional volume

Jasemin Ayse Ölmez¹ · Benjamin Busch¹ · Christoph Hilgers¹

Received: 31 July 2023 / Accepted: 29 March 2024 / Published online: 5 May 2024
© The Author(s) 2024

Abstract

The Upper Cretaceous limestones unconformably overlie Upper Carboniferous coal-bearing lithologies and are studied to assess their effect on rising mine-water levels in the Ruhr mining district. Upper Cretaceous sedimentary rocks from the Münsterland Cretaceous Basin have previously been studied regarding their sedimentary structures and fossil content. However, understanding the petrophysical and petrographic heterogeneity in regard to sedimentary properties and their effect on fluid migration pathways is yet missing. Utilizing He-pycnometry, Klinkenberg-corrected air permeabilities, p-wave velocities, transmitted and reflected light analyses, point-counting and cathodoluminescence, we assess the petrophysical, geomechanical and mineralogical properties. Porosity ranges from 1.0 to 18.7% and permeability ranges from <0.0001 to 0.2 mD, while p-wave velocity ranges between 2089 and 5843 m/s. Mechanical compaction leads to grain rearrangement, deformation of calcispheres, foraminifera and ductile clay mineral laminae. Above and below clay laminae, compaction bands of deformed calcispheres develop. Early diagenetic mineral precipitation of ferroan calcite in inter- and intragranular pores reduces porosity and permeability and influences geomechanical properties. An underestimated aspect of limestone petrography is the relationship of the original primary compactable depositional volume and the influence of compaction, deformation and cementation during early and late diagenesis on reservoir properties. The detrital dominated limestones show an originally high compactable depositional volume (CDV). Overall, reservoir qualities are poor and indicate the sealing potential of the studied lithologies. The Upper Cretaceous (Campanian) limestones thus may act as a barrier for increasing mine-water levels from dismantled, post-mining subsurface hard coal mines in the region.

Keywords Upper Cretaceous · Münsterland Cretaceous Basin · Reservoir quality · Diagenesis · Cementation · Calcispheres

Introduction

Carbonate rocks have very heterogeneous reservoir properties from bed to reservoir scale (Lucia et al. 2003; Ehrenberg and Nadeau 2005; Rashid et al. 2017). The reservoir properties rely on depositional, diagenetic and structural modification (Worden et al. 2018). Usually, the reservoir quality of a formation is determined to identify porous and permeable lithologies, e.g. for oil and gas exploration, carbon capture and storage (CCS) or geothermal use-cases (Choquette and Pray 1970; Amthor et al. 1994; Ehrenberg 2006; Ehrenberg

et al. 2006; Ahr 2008; Armitage et al. 2013; Abuamarah and Nabawy 2021). Since the reservoir quality is influenced by diagenetic modification (compaction, mineral precipitation, alteration and dissolution) and the fracture network, an understanding of controlling factors and anisotropies is important. Understanding the diagenetic overprints in Cretaceous sediments as sandstones and limestones is important for the successful exploration of a reservoir or storage potential for gas sequestration and were studied, e.g. in Abu Dhabi (Morad et al. 2019), in the Amposta offshore oil reservoir in Spain (Playà et al. 2010) and in China (Xi et al. 2015). However, macro- and microscale natural fractures additionally influence the reservoir or sealing potential of carbonate rocks (La Bruna et al. 2020). Although carbonate turbidite systems are heterogeneous, fractured carbonate turbiditic deposits can be of interest, e.g. for oil and gas production (Coffa et al. 2015).

✉ Jasemin Ayse Ölmez
jasemin.oelmez@kit.edu

¹ Structural Geology and Tectonics, Institute of Applied Geosciences, Karlsruhe Institute of Technology (KIT), Adenauerring 20a, 76131 Karlsruhe, Germany

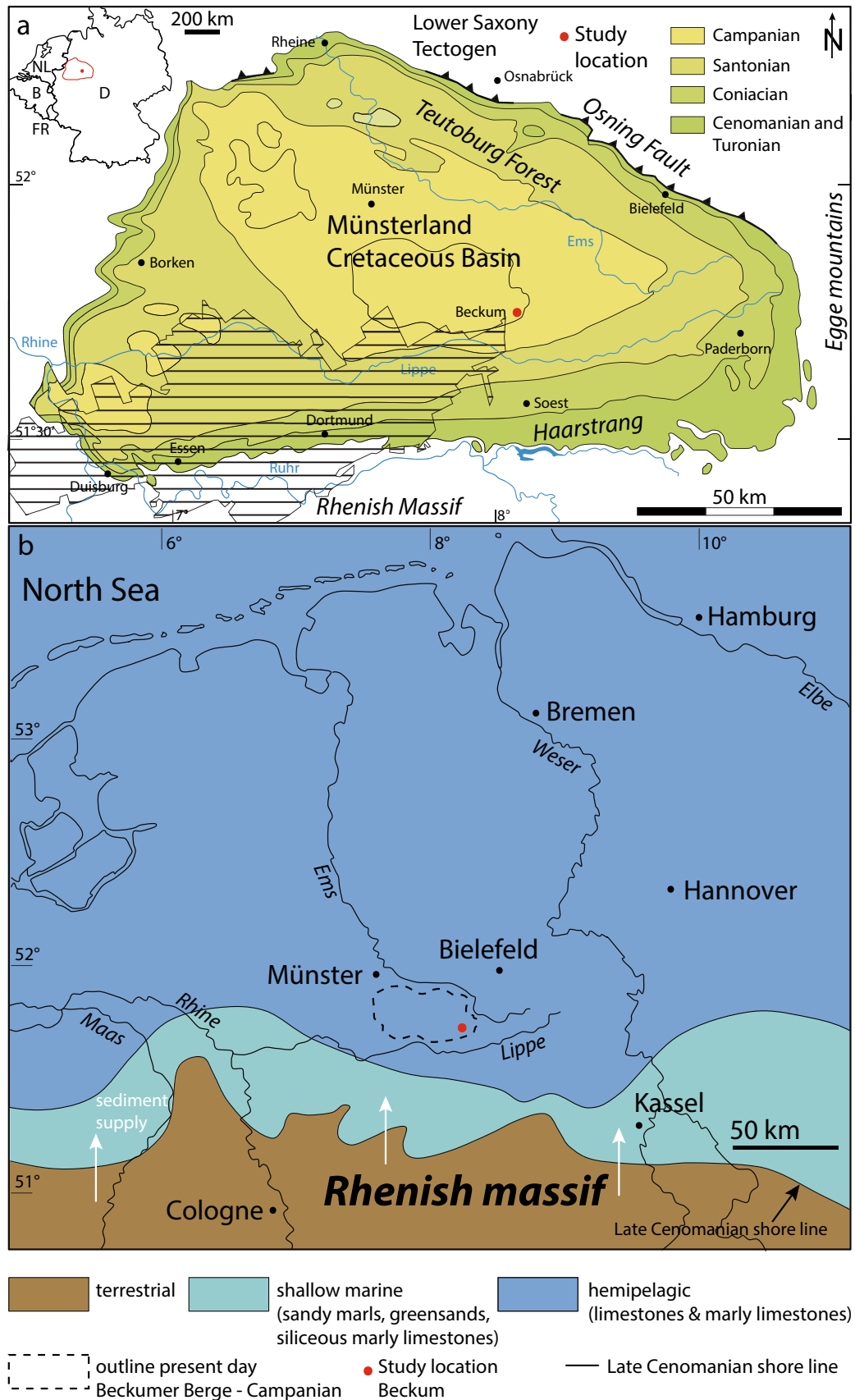


Fig. 1 **a** Simplified stratigraphic overview of the Münsterland Cretaceous Basin; the study location Beckum is marked in red. Limestones, claystones/shales and marlstones are exposed and mined for the cement industry (modified after Hiss and Mutterlose 2010; Janetschke and Wilmsen 2013 and references therein; Drozdowski and Dölling 2018). The red box displays the Münsterland Cretaceous Basin, the red dot marks the approximate location of the study area in Germany (Beckum) and the hatched area marks the distribution of former hard coal mines (Wirges and Dodenhoff 2019; Geologischer Dienst NRW 2020), D—Germany, B—Belgium, FR—France, NL—Netherlands. **b** Paleogeographic map of the North German Basin area and the present-day outline of the approximate study location (red dot) in the Beckumer Berge with possible terrestrial sediment supply (white arrows) from the Rhenish massif during the late Cenomanian, modified after Hiss (1995) and Erbacher et al. (2020)

This study aims to determine the porosity and permeability as well as their controlling factors as the Upper Cretaceous limestones unconformably overly Upper Carboniferous coal-bearing strata. The Upper Cretaceous deposits are discussed to be sealing lithologies on top of the northernmost extent of the former coal mining district (Fig. 1a), which are discussed to decouple the rising mine-water levels or gas seepages from the ground water since the cessation of coal mining in Germany (Rudolph et al. 2010; Coldewey and Wesche 2017). The sedimentary rocks of the Upper Cretaceous in the Münsterland Cretaceous Basin have so far mainly been studied in lithological and paleontological terms (e.g. Giers 1958; Arnold et al. 1960; Voigt and Häntzschel 1964; Kappel 2002; Wilmsen et al. 2019; Püttmann and Mutterlose 2021). The stratigraphic sequences of the Campanian rocks were determined by Giers (1958), Wolf (1995), Kaplan (2004) and Kappel (2002) using detailed regional designations. Prior mineralogical analyses have mainly been carried out to determine mineable formations for the cement industry. However, limited research has focused on the diagenetic parasequence and petrophysical properties of the studied lithologies. An under-researched aspect in this region is therefore the small-scale distribution of petrographic and petrophysical heterogeneities and their influence on the reservoir rock as well as the relation to the fracture network. Since compaction and diagenesis influence porosity and permeability, a detailed investigation of the petrographic and petrophysical properties can identify controlling factors for reservoir properties. Here, we determine the reservoir quality and the diagenetic parasequence to assess the impact of diagenesis and compaction on the compactable depositional volume. For this purpose, outcrop analogues were studied and sampled. Outcrop analogues also provide information on lateral layer continuity, the fracture network and their influence on the fluid flow on the basin scale. Results can be applicable to assess the interaction of rising mine-water and outline future potential for regional geothermal use of the formation.

Geological setting

The study location is in the opencast mine of Phoenix Zementwerke Krogbeumker GmbH & Co. KG in Beckum, NW Germany. Beckum is located in the southeast of the Central Münsterland Cretaceous Basin and exposes Upper Cretaceous (Campanian) marlstones, claystones/shales and limestones of the Beckum Member. The Münsterland Cretaceous Basin itself contains Lower Cretaceous to Upper Cretaceous deposits and is surrounded by the Osning fault in the north/northeast, the Egge mountains to the east and the Haarstrang to the south. The basin opens towards the Lower Rhine Embayment in the west/northwest (Fig. 1a, b).

During the late Cretaceous, Europe was influenced by compression and deformation events of the Central European Basement, resulting in basement shortening and anticline uplift and folding and inversion of normal faults (Voigt et al. 2021 and references therein). The North Atlantic rift in conjunction with a tectonically induced regression at the transition from the Upper Jurassic to the Lower Cretaceous, based on the subsidence of the Lower Saxony Basin during transtensional tectonics, led to a change in sedimentation in Northwestern and Central Europe (Vejbæk et al. 2010). During the Cretaceous, smaller transgression and regression events occurred, and NW–SE to W–E compressional directions affected NW Europe (Kley and Voigt 2008). The long-term sea level during the Cretaceous had a maximum at 100 ± 50 m (Miller et al. 2005). Increased crustal extension of the Atlantic leads to intensive rifting and subsidence in the Central European Basin System, e.g. in the Lower Saxony Basin until the end of the Aptian (ca. 125–115 Ma) (Mazur and Scheck-Wenderoth 2005; Vejbæk et al. 2010). The South Atlantic Ocean opening resulted in a drift of the African Plate northwards and compression transfer to the Iberian-Peninsula to Europe (Voigt et al. 2021). Furthermore, Africa shifted relatively ESE to Europe (ca. 120 Ma), which caused a sinistral strike-slip movement along the plate boundary (Kley and Voigt 2008). During the Santonian (ca. 84 Ma), Africa drifted in a NE direction (Kley and Voigt 2008) and led to a compression towards the NE in Central Europe, which caused the inversions of NW–SE striking basins and increased subsidence (cf. Dölling et al. 2017). The southern edge of the inverted Lower Saxony Basin is represented by the Münsterland Cretaceous Basin (Voigt et al. 2021). As a result, the Late Cretaceous basement thrusts and inversion basins are formed as intraplate structures due to the weak lithosphere resulting from the Variscan orogeny and the overlying Palaeozoic to Mesozoic extensional basins (Kley and Voigt 2008). The NW–SE striking uplift and overthrust in the intraplate area is the result of the beginning of the Africa–Iberia–Europe convergence (Kley and Voigt 2008). NW–SE-oriented overthrusting of the Lower Saxony Tectogen onto the Münsterland

Cretaceous Basin led to curvature and partial overthrusting of the Cretaceous formations in the Teutoburg Forest (Wulff et al. 2017).

Upper Cretaceous clastic and carbonate sediments were deposited into a shallow basin north of the Rhenish Massif (Fig. 1b) (Wilmsen et al. 2019; Erbacher et al. 2020). In general, the thickness of the Upper Cretaceous sediments reaches up to 2,000 m in the north of the basin and 500 m at the southern margin due to low sedimentation rates and formation gaps (Scheck-Wenderoth et al. 2008; Voigt et al. 2021). The thickness distribution of the Upper Cretaceous in the Central European Basin System shows a dominance of NW–SE striking structural pattern, e.g. reactivation of faults due to inversion with local WNW–ESE striking folds and thrusts (Scheck-Wenderoth et al. 2008). From the western margin of the Ruhr area in Duisburg to the Paderborn Plateau in the east (Fig. 1a), the shallowly north-dipping rocks of the Münsterland Cretaceous Basin unconformably overlie the folded Upper Carboniferous of the Ruhr and Sauerland regions. The youngest deposits are present in the centre of the Münsterland Cretaceous Basin (Beckumer Berge and Baumberge) and are exposed from old to young from Stromberg, Beckum and Vorhelm Members, which are to date combined in the Ahlen-Formation (Ahlen-Fm.) (STD 2016). The Lower Campanian consists of the Stromberg Member, comprising bioturbated grey limestones and marls with a mottled background. Slightly pronounced gradations indicate turbiditic fillings. Parallel to the strata, horizontally to obliquely bedded glauconitic, sandy limestones may occur (cf., Giers 1958; Kappel 2002; Wilmsen et al. 2019). The Upper Campanian starts with the Beckum Member, consisting of alternating limestone–marly shale sequences with a thickness of up to 25 m (Giers 1958). The limestone banks are deposits of debrite and turbidite flows and separated by thin (<0.2 m) claystone/marlstone to marly shale layer (Wolf 1995; Kaplan et al. 1996; Kappel 2002; Kaplan 2004). The overlying Vorhelm Member consists of a limestone–marlstone or marly shale alternation sequence with a total thickness up to 80 m (Giers 1958), showing no marker horizons and lateral inhomogeneities (Kappel 2002). In general, the Campanian lithologies in the Münsterland Cretaceous Basin are described as allochthonous sediments, resulting from debris flows, turbidites or submarine slumping (Giers 1958; Wolf 1995; Kaplan et al. 1996; Kappel 2002).

Materials and methods

In the Phoenix quarry in Beckum, a total of ~17.5 m limestone–marly shale alternations were recorded on successive vertical walls. Samples were taken from each limestone layer. In addition, samples were also taken from the vicinity of a fault zone to assess the influence on petrophysical and

petrographic properties. Rock classification in the field was performed according to Dunham (1962) and is supplemented by microscopic classification after Folk (1959) and Dunham (1962). For the fracture strike orientation, images were taken with a Mavic 2 Enterprise drone on a plane surface on the highest strata of the quarry. The fracture pattern was analysed and plotted with FracPaQ using the workflow from Healy et al. (2017).

For the petrophysical analysis, a total of 74 plug samples were drilled parallel and perpendicular to stratification from a hand specimen using a water-cooled 1-inch (~2.54 cm) core drill. The trim ends of the plugs drilled parallel to the stratification were used for thin section preparation. The plugs were dried at 40 °C in a drying oven for one week until weight constancy. Helium porosity and grain density were determined using a Micrometrics AccuPyc II 1340 pycnometer (e.g. Monsees et al. 2021). The Klinkenberg-corrected intrinsic permeability measurements were carried out with an air permeameter from Westphal Mechanic using dry, oil-free laboratory air (80% N₂, 20% O₂) as permeant at 1.2 MPa confining pressure to avoid sample bypassing (e.g. Klinkenberg 1941; Rieckmann 1970; Schmidt et al. 2021). The measurement range for the device is between 0.0001 and 10,000 mD ($1 \text{ mD} \triangleq 9.869 \times 10^{-16} \text{ m}^2$). Ultrasonic pulse velocity measurements were carried out using a Proceq Pundit 200 ultrasound system with two 54 kHz transducers at 200 V pulse voltage and 50× receiver gain. The longitudinal wave (p-wave) was determined by measuring the transit time t_0 (μs) via the longitudinal axis of the plugs and converted into the wave velocity (v_p ; m/s). A coupling gel was used for direct and soft contact with the plugs. The measurement frequency depends on the sample diameter. For samples with a diameter of 2.54 cm, the frequency has to be below 1 MHz to secure physical consistency (Kummerow 2006).

A total of 49 samples were embedded in blue dyed epoxy resin to highlight porosity and were used to prepare thin sections with a thickness of 30 μm. Thirty-five of these thin sections were stained with a combined solution of alizarin red S and potassium ferricyanide (Dickson 1965) in 0.3% HCl on one half of the thin section to distinguish different carbonate phases and covered with a glass cover slip. Calcite will stain reddish (pink, orange) and ferroan calcite will stain blue, while dolomite remains unstained (Dickson 1965). The remaining 14 thin sections were polished for further microscopic analyses. A Leica DMLP and a Progres Gryphax camera system were used for petrographic examination. Polished thin sections were also examined using cold cathode cathodoluminescence (CITL CL8200 Mk5-2 Optical Cathodoluminescence System mounted on a Leica DIALUX 20 ES) (e.g. Monsees et al. 2020) in a low vacuum <0.001 mbar, at an acceleration voltage of 10.3 kV and a current of 325 μA to distinguish different cement phases and zonations. Opaque minerals were analysed by reflected light microscopy on polished thin sections with a

Leitz OrthoplanP and a Progres Gryphax camera system using oil immersion. For the grain size determination of the calcispheres, at least 100 grains were measured in each thin section with ImageJ on a grid adjusted to the largest observed grain size to gain area weighted results (e.g. Becker et al. 2017). The width of clay laminae, compaction bands and veins were also measured using ImageJ. For micrite ($\leq 4 \mu\text{m}$) and microsparite (5–10 μm), grain size values by Folk (1959) and Folk (1974) were used. As the grain size could not be determined during point-counting, the distinction between micrite and microsparite was not possible; therefore, the term micrite is used. Point counts were performed on 300 points using a Pelcon semi-automatic point counter installed on a Leica DMLP microscope using a step-length adjusted to the maximum observed particle size (e.g. Busch et al. 2019) of 100 μm . The porosity types were determined according to Choquette and Pray (1970). The compaction of the calcispheres was further determined following Fry's method (Fry 1979) using ImageJ. To determine the compaction ratio, horizontal (long) and vertical (short) lengths of the calcispheres were measured, but were only recorded in the vicinity of the clay mineral laminae.

Compactable depositional volume

The concept of 'compactable depositional volume (CDV)' was introduced to determine the volume loss as a function of compaction prior to cementation. The CDV is the volume that is potentially compactable after deposition and before the formation of authigenic cements similar to the intergranular volume (IGV) commonly used in sandstones (Houseknecht 1987; Paxton et al. 2002). The CDV is the sum of interparticle porosity, intraparticle porosity, microporous clay and micrite and all authigenic phases, which precipitated in primary pores (including intraparticle pores) (Eq. 1). Just as the IGV, it measures the amount of intergranular porosity and pore-filling cements. In contrast to IGV, however, carbonate rocks often contain porous fossils, which may break or compact. Thus, the CDV also considers intraparticle porosity. This may aid in further assessing the degree of compaction in carbonate rocks within samples of the same lithology, especially when distinguishing inter- and intraparticle porosity, while also capturing the stabilizing effects of authigenic phases.

CDV (%)

$$\begin{aligned}
 &= (\Sigma \text{Interparticle porosity}(\%) + \Sigma \text{Intraparticle porosity}(\%) \\
 &\quad + \Sigma \text{Interparticle cement}(\%) + \Sigma \text{Intraparticle cement}(\%) \\
 &\quad + \Sigma \text{Micrite}(\%) + \Sigma \text{Clay laminae}(\%))
 \end{aligned}
 \tag{1}$$

As this indicator calculation also includes microporous micrite and clay mineral laminae, it is possible that the value does not reach 0%, but samples rich in micrite or clay mineral laminae will show high CDV, which can still be correlated

to high microporosity contents. Similarly, sandstone samples containing abundant depositional clay mineral matrix will also show high IGV values (Paxton et al. 2002). In samples which contain abundant porous particles (e.g. calcispheres), the presented approach can aid in comparing the effect of compaction, as uncompacted samples will have higher CDV than compacted samples. However, just as the IGV, the CDV is not directly comparable to the petrophysically measured He-porosity, as intraparticle cements can fill cavities within porous particles, reducing the porosity, while stabilizing the particle itself against compaction. Therefore, this point-count-based calculation enables the comparison of the state of compaction within a lithology and its relation to assessed reservoir properties.

Results

Lithology

The lithological profile contains alternating, layered argillaceous limestones to calcareous marlstone and marlstone to claystone or marly shale deposits of varying thicknesses (Fig. 2). The total recorded lithological thickness is ~17.5 m. Due to further simplification, the terminologies limestone and marly shales are used. The marly shale layers are dark grey, finely bedded and up to 1.6 m thick at the upper level, but generally are <0.2 m thick. Overall, a fining-upwards trend is recognizable; the marly shale bed thickness increases towards the top, while the limestone beds recede (Fig. 2 and Fig. 3a, b). The limestones and marly shales are both fine-grained and the limestones are classified as mudstones to wackestones after Dunham (1962). Firm, dark, claystone to marly shale layers (approx. 5 cm thick), which occur at irregular intervals between the limestones and marly shales, are apparent. The observed fault (Fig. 3c) was characterized as a normal fault using slickensides. Some of the fracture surfaces show a brownish to yellowish coating, which is due to iron hydroxide precipitation associated with alteration of idiomorphic pyrite and marcasite in the formation. One well-preserved belemnite was found at about 2.6 m (Fig. 2), which was determined as belemnite *mucronate* due to its slenderness. In higher strata (Fig. 2), two belemnite fragments were found, but could not be classified because of missing morphology information.

Structure

Three main fracture orientations were obtained from the drone imagery evaluation, showing three main sets striking WSW–ENE, NNE–SSW and NW–SE (Fig. 4). Fractures are partly continuous, penetrate limestone and marly shale layers

or are interrupted during layer changes, but open fractures (mm range aperture) are only rarely found.

Petrography: texture

The average size of the calcispheres is 0.042 mm (avg. range 0.038 to 0.044 mm). For micrite-dominated layers, the average grain size is limited by the maximum grain size (0.004 mm) per definition after Folk (1959); Folk (1974). The well-rounded calcispheres with a calcitic test appear evenly distributed (Fig. 5a) and as elongated rock fragments within the micritic matrix (Fig. 5b). The calcispheres (stained red) are partly deformed around clay laminae (Fig. 5c, d), and rarely broken (Fig. 5e). By microscopical analyses, the limestones are classified as wackestone to packstone according to Dunham (1962). Grains as detrital quartz, glauconite and some unstained carbonate grains have a rounded to elliptical shape, but are not aligned parallel to bedding.

Detrital composition

The most abundant detrital component is micrite with an average content of 51.5% (min.: 17.7%, max.: 88.0%). The second most abundant are calcispheres with an average content of 16.4% (min.: 0.0%, max.: 34.7%). The third most abundant are clay minerals in laminae (avg.: 4.8%, min.: 0%, max.: 22.7%). In addition, different foraminifera types (avg.: 1.2%, min.: 0%, max.: 4.0%), detrital quartz and chert grains (avg.: 0.2%, min.: 0%, max.: 2.7%), test or shell fragments (avg.: 0.8%, min.: 0%, max.: 3.3%), unidentified carbonate grains (avg.: 0.2%, min.: 0%, max.: 2.7%), phosphate grains (avg.: 0.3% min.: 0%, max.: 1.0%), glauconite (avg.: 0.4%, min.: 0%, max.: 2.0%), micrite in calcispheres (avg.: 0.1%, min.: 0%, max.: 2.0%), dolomite rhombs (avg.: 0%, min.: 0%, max.: 1.0%), bivalves (avg.: 0%, min.: 0%, max.: 0.3%), undifferentiated fossils (avg.: 0%, min.: 0%, max.: 0.3%) and micrite in foraminifera (avg.: 0.0%, min.: 0.0%, max.: 0.3%) are recorded (full sample table in supplementary materials). In total, the detrital composition varies between 51.7% and 94.0% (avg.: 76.3%).

Micrite, calcispheres, test and shell fragments, foraminifera and other microfossils in this study are primarily composed of calcite, as indicated by the red stain (Fig. 5a, e), while only individual foraminifera have a dolomitic composition and remain unstained (Fig. 5f). Dolomite occurs rarely as single rhombic crystal within the micrite matrix. Chert occurs as yellow grains or as silicified shell fragments and show small microcrystalline spheroids with crossing extinction. Glauconite is found occasional in thin sections as rounded grains (Fig. 5c). The detrital composition in limestones varies with the calcisphere content and the position along the lithological profile. If the calcisphere content decreases, the micrite content increases (cf., Fig. 2). In younger strata, where clay

laminae are mostly missing, the micrite matrix is densely packed and individual calcispheres are deformed both in a ductile way and locally crushed. In general, the calcisphere content decreases towards the top of the studied section (cf., Fig. 2). Calcispheres are also found as parts of densely packed clasts, which are partially aligned to the bedding direction (Fig. 5b). Surrounding clay laminae, calcispheres often appear deformed in a ductile way (Fig. 5c, d). The clay laminae thickness varies between 0.04 and 0.37 mm (avg.: 0.16 mm). Cemented calcisphere clasts occur occasional with an average length of 1.08 mm (min.: 0.24 mm, max.: 2.09 mm).

In a single layer at ~12.5 m (Fig. 6) consisting mainly of clay and micrite, partially or completely dissolved peloids/pellets with an average size of 0.35 mm (min.: 0.2 mm, max.: 0.49 mm) occur frequently. They contain fossil fragments or pyrite and are crosscut by most likely (ferroan) calcite veins (Fig. 6a, b). In stained thin sections, the remnants of the peloids/pellets remain unstained, indicating a dolomitic composition.

Authigenic composition

The most abundant authigenic minerals are sparry ferroan calcite, which precipitated in the calcispheres (stained blue, avg.: 10.4% min.: 0%, max.: 23.3%). The second most common authigenic mineral is pore-filling ferroan calcite, e.g. within the micrite matrix (avg.: 6.9%, min.: 0%, max.: 27.0%), while the third most abundant are unstained pore-filling carbonates (avg.: 1.7%, min.: 0%, max.: 10.3%). Other authigenic minerals include pore-filling calcite (avg.: 1.3%, min.: 0%, max.: 6.7%), sparry ferroan calcite in foraminifera chambers (avg.: 0.5%, min.: 0%, max.: 2.3%), (ferroan) calcite and strontianite vein cements (avg.: 0.4%, min.: 0%, max.: 10.0%), pyrite/marcasite in calcispheres (avg.: 0.3%, min.: 0%, max.: 5.3%) and in clay laminae (avg.: 0.2%, min.: 0%, max.: 1.3%). Pore-filling green clay minerals (avg.: 0.7%, min.: 0%, max.: 2.7%), sparry ferroan calcite in bivalves (avg.: 0%, min.: 0%, max.: 0.3%), clay minerals in calcispheres (avg.: 0.0%, min.: 0.0%, max.: 0.3%) and clay minerals in foraminifera (avg.: 0.0%, min.: 0.0%, max.: 0.3%) reflect minor authigenic minerals. In total, the authigenic composition varies between 6.0 and 48.3% (avg.: 23.4%).

Blue-stained sparry ferroan calcite fills the inner part of calcispheres or other fossils and most veins (Fig. 5a). Pore-filling green clay minerals and green clay minerals in fossils most often coat the inside of individual fossil tests (Fig. 5a). Where the fossils or calcispheres are broken, further sparry ferroan calcite cements are also encasing the broken fragments (Fig. 5g). Pervasively sealed veins (Fig. 5a, h) are composed of an intergrowth of ferroan calcite (stained blue) and calcite (stained red, Fig. 5a). This mineral paragenesis will be abbreviated as (ferroan) calcite. Narrow veins show a width from 0.012 to 0.05 mm (avg.: 0.026 mm), while

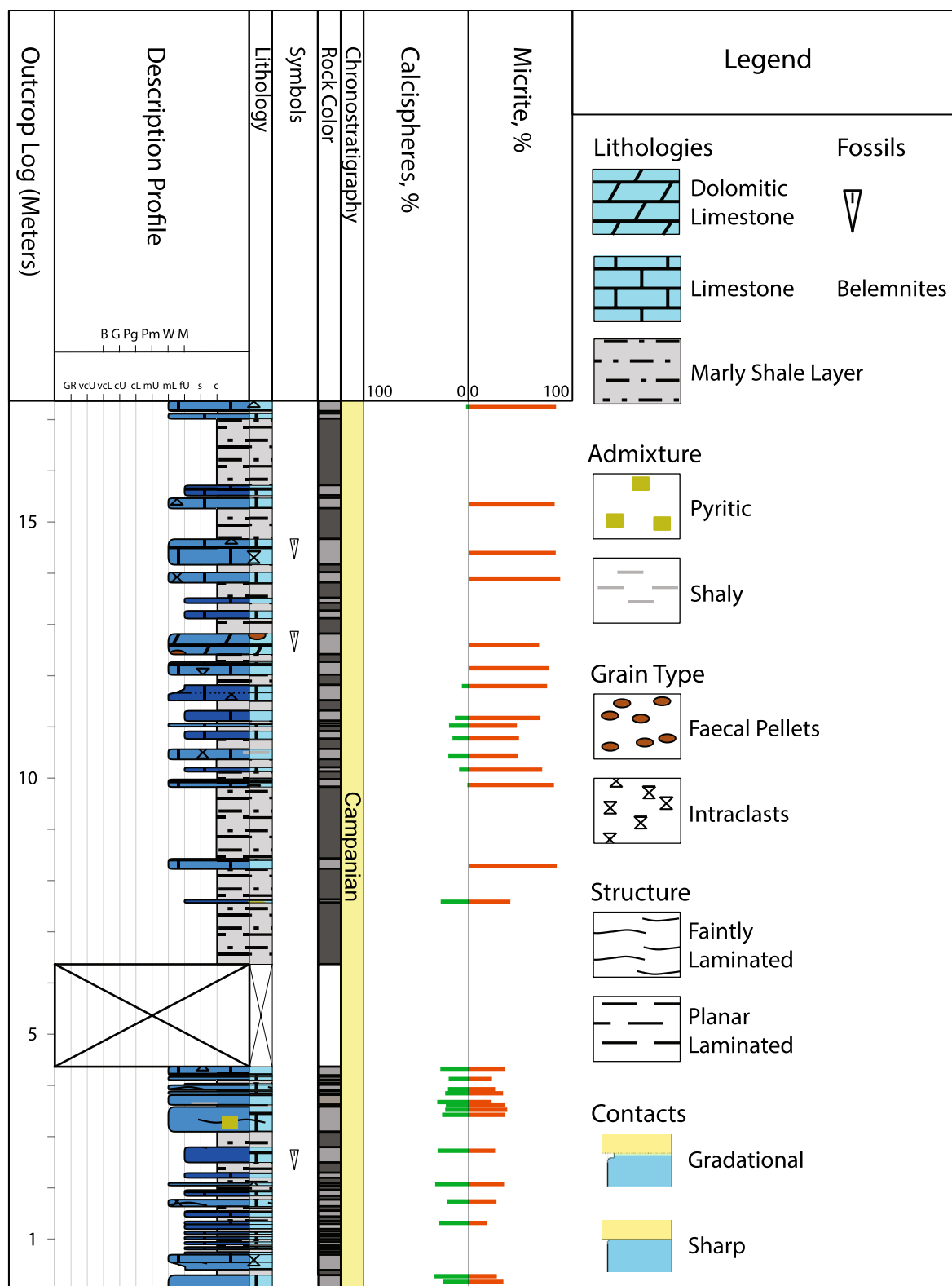


Fig. 2 Stratigraphic column including grain size distribution and petrographic data (point-counting data for calcspheres and micrite content). Faintly laminated limestones are in the lower studied part, inter-

bedded with marly shale layers. A fining-up trend is noted towards the top. In addition, faintly laminated limestones are predominant in the lower section. Missing part is marked by a white box

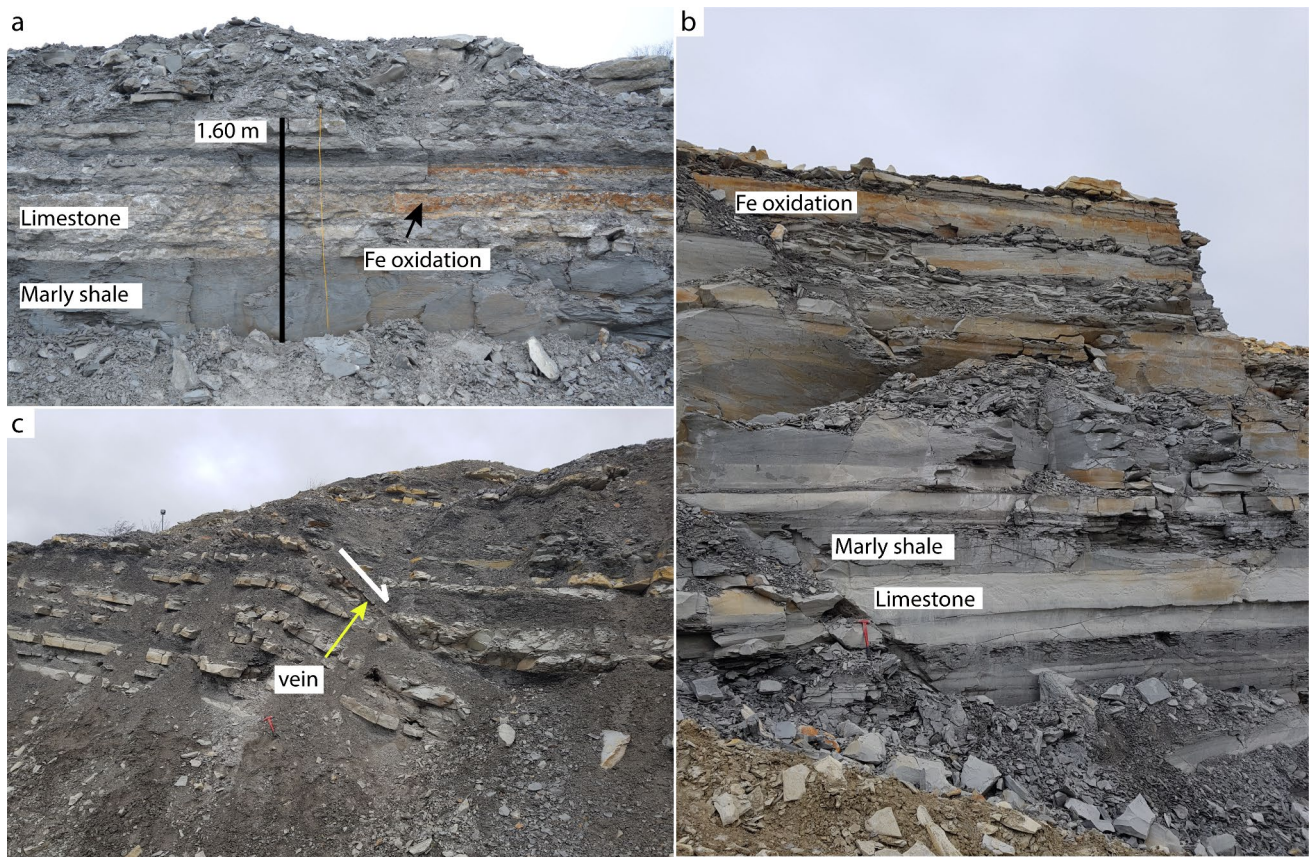


Fig. 3 Overview parts of the studied outcrop with different wall sections. **a** The lower part of the studied lithologies hosts limestone–marly shale alternations. The faintly laminated limestone surfaces are rough, and the interbedded marly shales are of varying thickness and occur as thinner or thicker beds (e.g. in the lower part of Fig. 3a). The limestone surface is partly coated with pyrite/marcasite and thus brownish to yellowish due to iron hydroxide precipitation. The wall

strikes W–E. **b** Portrait view, in strata above, the thickness of interbedded marly shale is increasing, and the limestones are no longer faintly laminated, but massive with even surface. The wall strikes NNW–SSE to NW–SE. **c** Fault zone with normal fault (white arrow) and (ferroan) calcite/strontianite vein (yellow arrow). The wall strikes NNE–SSW to NE–SW. Hammer for scale

wide veins around the fault show widths between 0.25 and 0.63 mm (avg.: 0.42 mm). Composite veins composed of (ferroan) calcite and strontianite were observed around the fault and within the undisturbed lithology (Fig. 6c, d). Composite veins of (ferroan) calcite and strontianite still retain open intercrystalline porosity between the strontianite crystals (Fig. 6d). Depending on the crystal section, strontianite can be fibrous to radiating spherulitic, bladed or botryoidal (Fig. 6d). They partly fill the remaining inner fracture porosity, which is outlined by euhedral crystal terminations of elongate blocky (ferroan) calcite crystals (Fig. 6d). In these composite veins, pyrite/marcasite is often present at the host rock–vein interface and encased in (ferroan) calcite. Also, a sheared (ferroan) calcite vein contains elongated host rock inclusions and remaining fracture porosity is filled by strontianite, where strontianite again retains intercrystalline porosity within the vein (Fig. 6d, Fig. 8). Larger strontianite or (ferroan) calcite/strontianite veins are found in samples from the fault zone and in samples PHX10, PHX26 and

PHX27. Pyrite and marcasite are mostly found surrounding or within clay laminae as framboids, within calcispheres and other fossils (Fig. 5d). The framboidal pyrite present in intraparticle pores of calcispheres and foraminifera is additionally encased in ferroan calcite in some samples (Fig. 5a, f, g).

Cathodoluminescence analyses show that the calcitic calcispheres show a bright orange luminescence and a dull luminescing centre, where they are filled by ferroan calcite. Narrow authigenic, syntaxial (ferroan) calcite veins (avg. 0.01 to 0.05 mm wide) show no consistent zonation but a rather dull orange luminescence or non-luminescence with individual areas of brighter luminescence (Fig. 7a, b). In wider veins (0.25 to 0.63 mm wide), the brightest orange zones occur at calcite crystal boundaries showing euhedral terminations, while the centre mostly exhibits a dull orange luminescence indicating the presence of ferroan calcite. At the transition from host rock to vein, the (ferroan) calcite crystals show syntaxial growth and growth competition

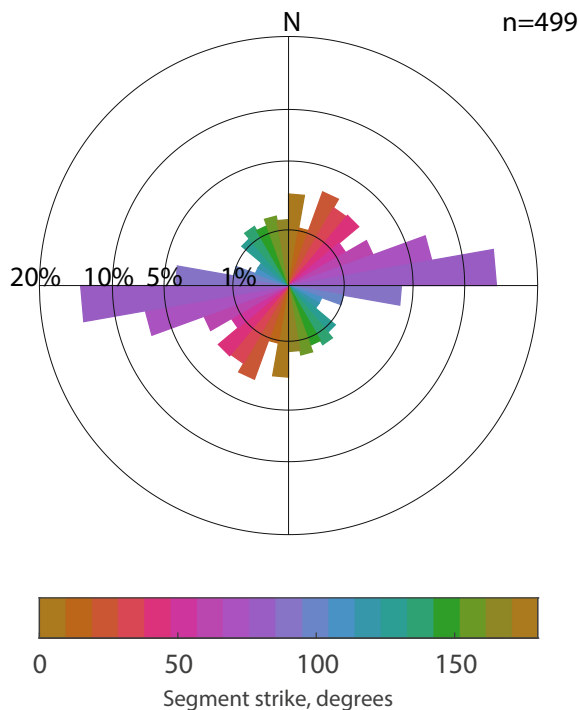


Fig. 4 Fracture data from drone imagery plotted as rose diagram (strike plot). Fracture data were generated using the FracPaQ workflow from Healy et al. (2017). Main striking sets from WSW–ENE, NNE–SSW and NW–SE

(Fig. 7b, c). In sample PHX10, the (ferroan) calcite vein cements precipitate syntactically on the host rock inclusions, and their crystal size increases towards the centre of the vein (Fig. 7b). In addition, the host rock inclusions appear to be cut again and are overgrown by an even larger syntactical (ferroan) calcite phase (top of Fig. 7b). The euhedral terminations of these crystals are again encased in strontianite (Fig. 7b). Strontianite shows a turquoise-bluish luminescence and zones of brighter and duller luminescence or non-luminescence in larger crystals (Fig. 7b, c, d). The micritic matrix generally shows a pale orange luminescence (Fig. 7 a, c, f), while only the sample containing a sheared vein shows a purple luminescence of the micrite both at the host rock–vein interface (Fig. 7d) and in the narrowly spaced (20–100 μm) host rock inclusions inside the vein (Fig. 7b, e). The peloids/pellets (interpreted as faecal pellets) encased in a micritic matrix show a reddish luminescence (Fig. 7f).

Optical porosity

Optical porosity is low with an average of 0.32% (min.: 0%, max.: 3.0%) and includes intergranular porosity (min.: 0%, max.: 1.0%) mostly between calcispheres and micrite, vuggy porosity in micrite (min.: 0%, max.: 1.0%), porosity in clay laminae (min.: 0%, max.: 0.7%), intraparticle porosity in

foraminifera (min.: 0%, max.: 0.3%) and intercrystalline porosity in veins (min.: 0%, max.: 3.0%). Secondary porosity is visible in PHX10, due to (partial) faecal pellet dissolution. Due to the low content, no point-counting data on secondary porosity of faecal pellets are available.

Compaction and deformation

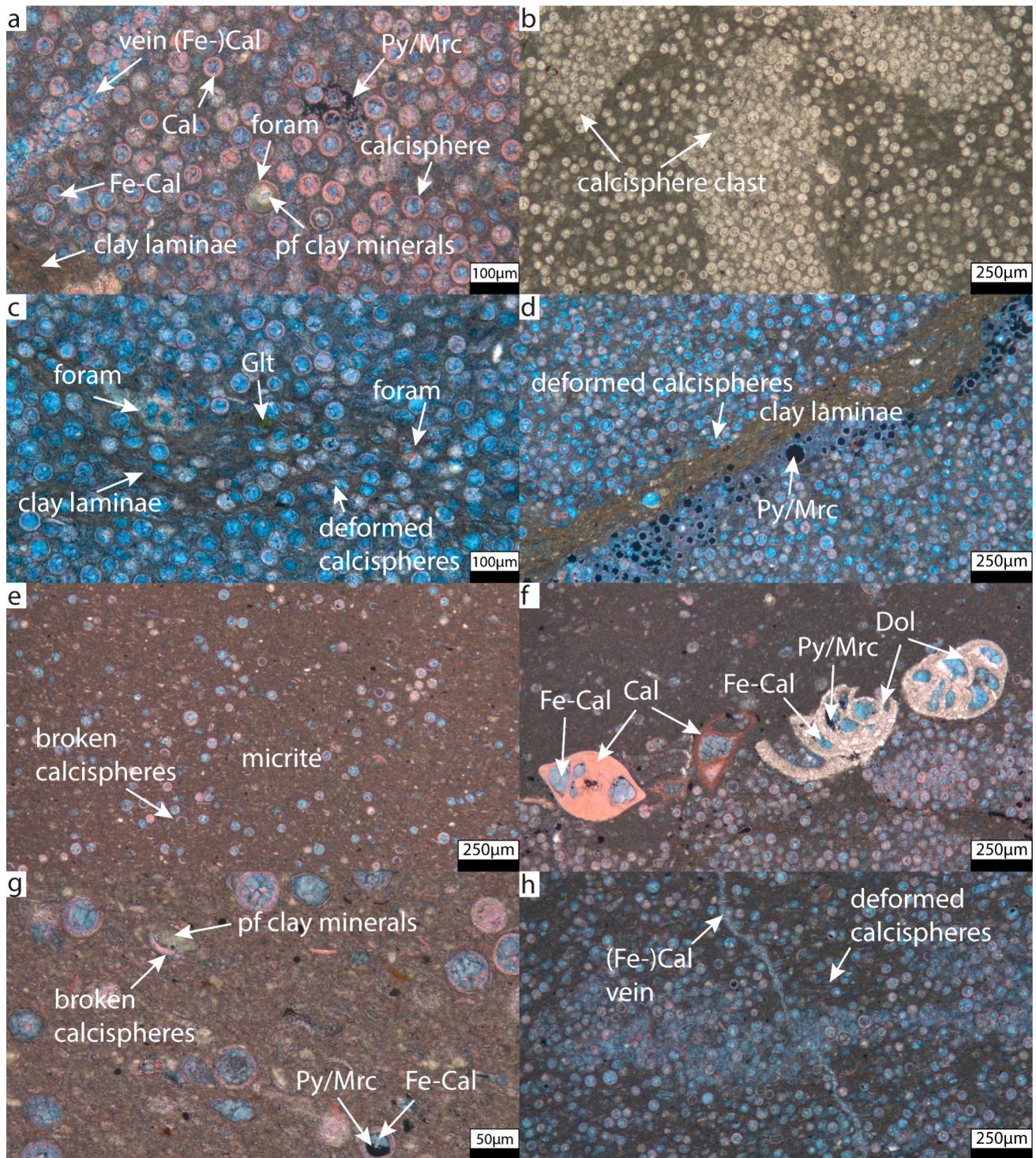
Compaction is recorded mainly by deformed calcispheres in contact with clay laminae and an absence of intergranular porosity. The calcispheres are partially pressed into the clay laminae and thereby elliptically deformed or even broke (Fig. 5c, d). This elliptical deformation allows the calculation of the degree of compaction with the Fry method (Fry 1979). The average ratio for undeformed calcispheres in areas lacking clay laminae 1.03 (min.: 0.97, max.: 1.14) and for deformed calcispheres within clay laminae is 1.82 (min.: 1.30, max.: 4.24) (PHX21–PHX34). Using ImageJ, the average thickness of the compaction bands formed by deformed calcispheres and clay laminae is 0.35 mm (min.: 0.26 mm, max.: 0.52 mm) (PHX24, PHX 26, PHX27, PHX33 and PHX34). The average vertical shortening measured on calcispheres around clay laminae is therefore 38.5% (min.: 4.5%, max.: 73.6%) and is restricted to the compaction bands formed by deformed calcispheres and clay laminae. No chemical compaction (e.g. stylolitization) was observed in the thin sections.

Compactable depositional volume

The compactable depositional volume (CDV) is the sum of potentially compactable volume after deposition and before diagenetic processes (which can cause the formation of cements in former pore spaces) and compaction (which can cause porosity and therefore volume loss due to grain rearrangement and fracturing of porous (micro)fossils). High CDV values thus represent samples, which retained most of this volume and could be less compacted than samples having lower CDV values. In this study, the CDV includes compacted (detrital) micrite; clay laminae; authigenic sparry ferroan calcite cements in calcispheres and foraminifera; pore-filling and intergranular calcite and ferroan calcite; calcite and unstained carbonate cements; clay minerals in calcispheres and foraminifera; pore-filling clay minerals in micrite; pyrite and marcasite in clay laminae, calcispheres or foraminifera; microcrystalline cement in calcispheres and all visible porosity in thin sections. In this study, the average CDV is 79.3% and ranges from 63.7 to 96.0%.

Petrophysical data

The He-porosity of the plugs drilled parallel to the stratification ranges from 1.0% to 18.7% (avg.: 8.1%). The grain density is 2.69 g/cm^3 to 2.85 g/cm^3 (avg.: 2.74 g/cm^3). The



He-porosity of the plugs drilled perpendicular to the stratification ranges from 1.2% to 14.7% (avg.: 7.7%). The grain density range is 2.68 g/cm³ to 2.78 g/cm³ (avg.: 2.74 g/cm³). For the fault zone, the He-porosities range from 4.1% to 9.9% (avg.: 6.0%) and grain densities from 2.73 g/cm³ to 2.78 g/cm³ (avg.: 2.74 g/cm³).

For plugs drilled parallel to stratification, permeability ranges from <0.0001 mD (technical measurement limit) to 0.201 mD (avg.: 0.0038 mD). For plugs drilled perpendicular to the stratification, the permeability ranges from <0.0001 mD to 0.079 mD (avg.: 0.0097 mD). The maximum values measured parallel to stratification are thus up to one order of magnitude higher than the plugs measured perpendicular to

Fig. 5 Photomicrograph showing **a** former hollow calcispheres which are cemented by ferroan calcite and also smaller veins are completely sealed by (ferroan) calcite (sample PHX34). Calcite is stained red and ferroan calcite is stained blue. However, also green clay minerals occur as filling in calcispheres or foraminifera. **b** Some thin sections showing clasts of reworked former calcisphere packstones (sample PHX30). Without staining, the distinction between calcite and ferroan calcite is not possible. **c** Calcispheres are deformed elliptical in areas where clay laminae are present, and glauconite occurs occasional (sample PHX27). **d** The appearance of pyrite/marcasite framboids is mostly limited to the vicinity of clay laminae or high clay content within the micritic matrix (sample PHX33). The opaque minerals occur either pore filling in fossils or dispersed in the clay laminae or the micritic matrix. **e** The upper lithologies consist mostly of micrite and clay (sample PHX12). **f** Dolomite or dolomitization of former fossils occurs sporadically (sample PHX19). **g** Reworked and broken fossils and tests are occurring within a more micrite and clay dominated matrix (sample PHX12). **h** Deformed calcispheres also occur at the transition to cemented calcisphere packstone clasts (sample PHX16). Cal: calcite, Fe-Cal: ferroan calcite, (Fe-)Cal: (ferroan) calcite, foram: foraminifera, pf: pore filling, Py/Mrc: pyrite/marcasite, Glt: glauconite, Dol: dolomite

the stratification. For the fault zone, the permeability ranges from <0.0001 mD to 0.0003 mD (avg.: 0.0002 mD). The p-wave velocity (v_p) of the plugs drilled parallel to the stratification ranges from 3333 to 5659 m/s (avg.: 4662 m/s). The v_p of the plugs drilled perpendicular to the stratification ranges from 2089 to 5843 m/s (avg.: 4230 m/s).

Correlations of petrophysical and petrographic properties

He-porosity and permeability values show no consistent correlation to each other (Fig. 9a). The correlation of grain density and He-porosity (Fig. 9b) indicates that porosity generally increases with higher grain density (parallel: $R^2=0.63$, perpendicular: $R^2=0.54$). Grain density (parallel: $R^2=0.52$, perpendicular: $R^2=0.45$) and porosity (parallel: $R^2=0.91$, perpendicular: $R^2=0.81$) both show a negative correlation with v_p (Fig. 9c, d).

In addition, porosity decreases with higher amounts of authigenic components (parallel: $R^2=0.30$, perpendicular: $R^2=0.59$) (Fig. 10a), while this correlation is more robust in samples prepared perpendicular to bedding. Porosity furthermore decreases with higher amounts of detrital calcispheres (parallel: $R^2=0.38$, perpendicular: $R^2=0.54$) (Fig. 10d), but increases with higher amount of total detrital components (parallel: $R^2=0.28$, perpendicular: $R^2=0.58$) and micrite (parallel: $R^2=0.43$, perpendicular: $R^2=0.67$) (Fig. 10b, c). Samples containing more than 4% clay laminae show a slightly positive trend with porosity and grain density (Fig. 11a, b), whereas the v_p decreases with a higher amount of clay laminae (Fig. 11c).

The CDV shows a negative correlation with the sum of authigenic components (Fig. 12a; $R^2=0.42$), a positive correlation with sum of the detrital components (Fig. 12b; $R^2=0.45$) and also a positive correlation with the amount

of micrite (Fig. 12c; $R^2=0.79$). The correlation of CDV and He-porosity indicates a generally positive correlation (Fig. 12d; parallel: $R^2=0.40$, perpendicular: $R^2=0.60$). Samples having lower present-day CDV values thus have lost more porosity and volume during compaction and thus have lower present-day porosity.

Discussion

Lithology and petrographic analyses

The alternation of pelagic, allochthonous limestone beds (argillaceous limestones to calcareous marlstone) with marly shale layers (claystone to marlstone) and an overall fining upward trend indicate turbiditic or debris flow deposits as also previously described by Kappel (2002). Turbidites and debrites often originate due to overload at slopes and slope failure or due to tectonic triggers, e.g. basin inversion, earthquakes or gravity driven flow (e.g. Dott 1963; Bouma 1964; Lowe and Guy 2000 and references therein; Bouma 2004). The presence of clasts composed of individual densely packed calcispheres could represent erosion and re-deposition by turbidity currents. As typical turbiditic sequence lithologies are not recognized in the studied lithologies, the layers can also be interpreted as debris flows with silt grain sizes. Due to the small grain size and high micrite content towards the top of the studied interval, the layers can also be interpreted as suspension flow in general (cf., Voigt and Hantzschel 1964). The visible fining upward trend in thin sections and field observations (Fig. 2, 3) may thus represent a combination of smaller sea-level fluctuations in combination with suspension flow. Furthermore, the absence of calcispheres at the top of the studied interval may be an indication for sea-level or environmental changes (e.g. Masters and Scott 1979; Vodrazkova and Munnecke 2010). In this case, the sedimentation rate may be controlled by the Late Cretaceous inversion (e.g. Voigt et al. 2021) and thus slumping (cf., Wolf 1995). The origin and transformation of carbonate muds and micrite is still an ongoing discussion (e.g. Munnecke et al. 2023), and detrital micrite can be classified as allomicrite (e.g. Wolf 1965; Munnecke et al. 2023). Micrite observed in this study was classified as detrital, as the lithologies are described as redeposited. But also, autochthonous micrite could be part of the lithologies, after redeposition, and thus the term allomicrite was not applied. Also, glauconite, phosphate and dolomite are classified as detrital due to the redeposition. Additional authigenic occurrence cannot be excluded.

Textures observed in thin sections and hand specimen from higher strata indicate rapid deposition, since fossils, e.g. foraminifera or test and shell fragments, are broken and do not show any preferential orientation (cf., Fig. 5e, g). The

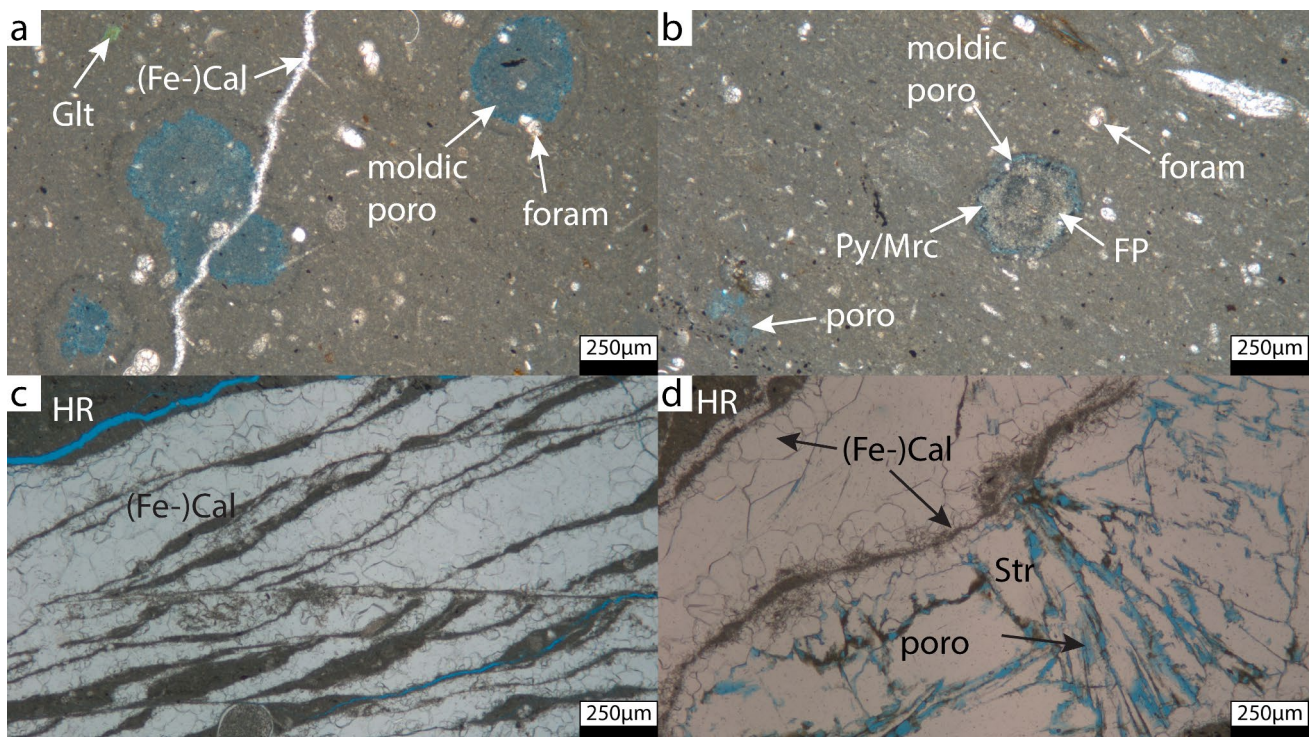


Fig. 6 **a** Photomicrograph showing micrite to clay matrix, containing smaller test or shell fragments, foraminifera and glauconite. Former pellets are completely or partially dissolved and therefore cause moldic porosity. A carbonate vein, most likely (ferroan) calcite, crosscuts the former pellet. **b** The pellets are roundish, and dissolution is more pronounced at the outline of the pellet. **c** Sheared carbonate (likely ferroan calcite) vein, which includes host rock material. **d** The syn-

taxial (ferroan) calcite vein is completely sealed and shows growth competition, whereas bladed to fibrous strontianite veins retain intercrystalline porosity (sample PHX10). foram: foraminifera, Glt: glauconite, moldic poro: moldic porosity, poro: porosity, (Fe-)Cal: (ferroan) calcite, HR: host rock, FP: faecal pellet; Py/Mrc: pyrite/marcasite, Str: strontianite

macroscopic fossil content is low; apart from three preserved belemnites, other macroscopic fossils are rarely present at the studied wall sections (Fig. 2). One belemnite was completely preserved and described as belemnite *mucronate*, due to its slenderness (Giers 1958; Kappel 2002). Based on the limestone–marly shale alternation, the calcispheres and foraminifera content, the identified belemnite and the overall rarely found macrofossils, the deposits can be interpreted to belong to the Beckum Member, in the transitional area of the Stromberg to the Beckum Member (c.f., Giers 1958; Kappel 2002). The transition to the Vorhelm Member in the hanging wall cannot be excluded.

The most abundant detrital components are micrite and calcispheres. They indicate deposition on a shelf in shallow to deep marine environment (e.g. Wilson 1975; Grobe and Machel 2002). Calcispheres are described as oligostegines (e.g. Giers 1958; Voigt and Häntzschel 1964; Kappel 2002) or calcareous dinoflagellate cysts in previous publications (e.g. Wendler and Willems 2004; Wiese et al. 2004). Also, the term calcisphere is described as ‘problematic’ by Versteegh et al. (2009), since the terminology and grouping is not clearly defined. In general, the abundance

of calcispheres in Cretaceous lithologies worldwide (Albian to Upper Campanian) is well known (e.g. Vodrazkova and Munneke 2010; Wendler and Bown 2013). As Cretaceous calcispheres are common between shallow-water and shelf-margin to slope deposits (e.g. Masters and Scott 1979), the depositional environment cannot be clearly classified by the calcispheres as an indicator. However, the association with mostly planktic foraminifera indicates a shelf-margin to slope deposit (Masters and Scott 1979). The observed roundish-to-elliptical peloids/pellets exhibiting dissolution porosity along their margins (Fig. 6 b) were interpreted as non-skeletal grains and because of the average grain size of 0.35 mm as peloids, which are partly or completely dissolved. Since they are not stained, a dolomitic composition is derived. Since some of the peloids also contain round structures, small opaque components or foraminifera fragments, the peloids are further interpreted as lithified faecal pellets (cf., Fig. 6a, b). Generally, faecal pellets preferentially occur in slope or shelf/ramp facies as well as deep water environments (Deik et al. 2019), and are therefore not considered as depositional indicators. Rarely occurring green clay minerals, filling intraparticle pores in foraminifera or calcispheres,

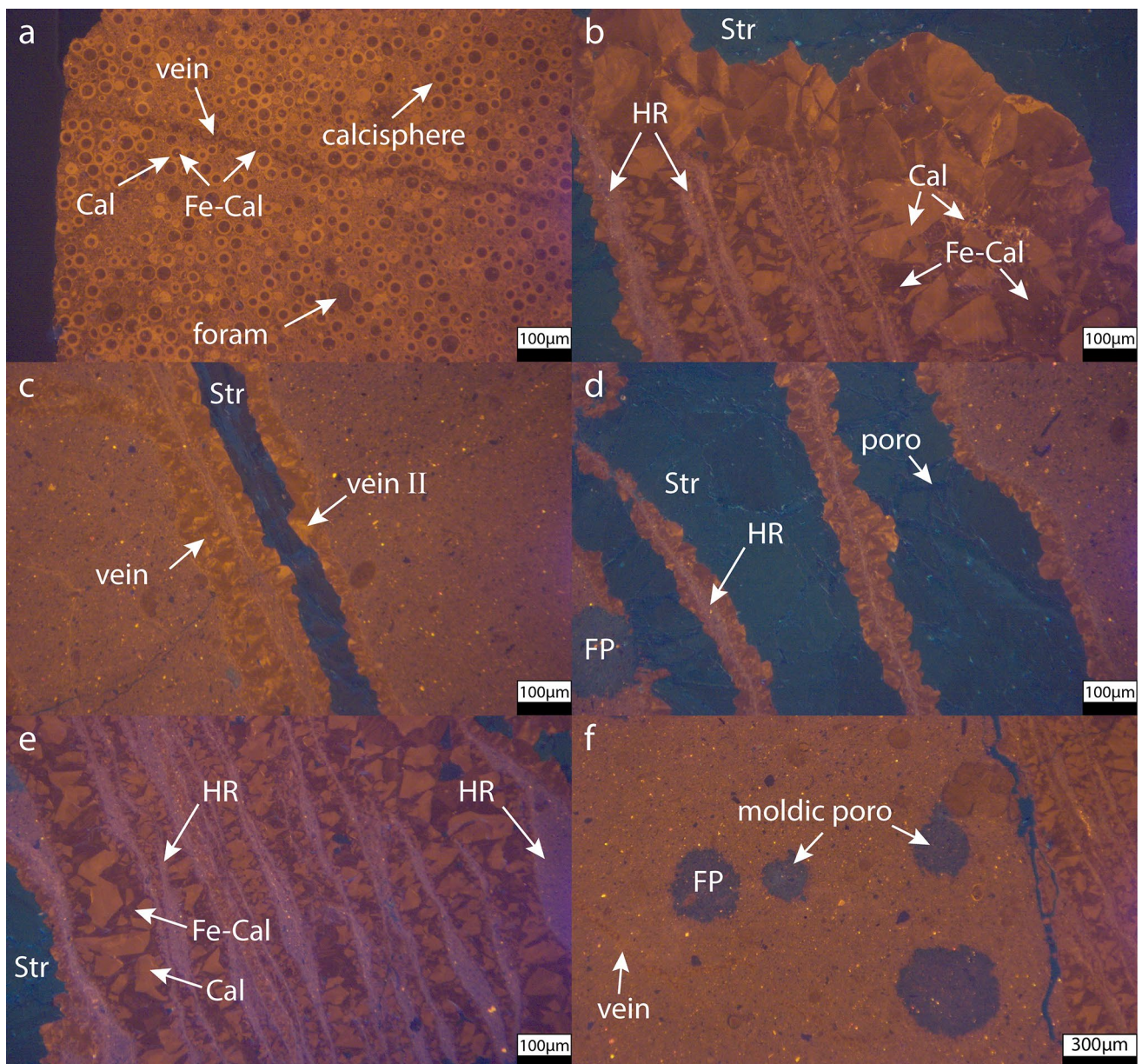


Fig. 7 Photomicrographs of cold cathodoluminescence showing different luminescence properties of calcite (Cal), ferroan calcite (Fe-Cal) and strontianite (Str). **a** Calcite shows bright orange luminescence colour, while ferroan calcite is dull (sample PHX34). Calcite occurs in the test of calcispheres or other fossils, while ferroan calcite cements occur as pore-filling cement or vein. The luminescence of micrite between the fossils is not as bright as pure calcite. **b, c** The wide veins contain zones of both bright and dull luminescence up to

non-luminescence calcite to ferroan calcite, while reactivated veins (vein II) also contain strontianite which shows a bluish luminescence (sample PHX10). Multiple parallel veins also contain host rock fragments (HR). **d** Larger strontianite veins also show zonation within the crystals with brighter and darker zones (sample PHX10). Faecal pellets (FP) are partially dissolved. **e** Host rock inclusions in (ferroan) calcite veins show a purple luminescence (sample PHX10). **f** Remaining faecal pellets show a reddish luminescence (sample PHX10)

and individual glauconite grains are interpreted to be redeposited, since all former pore spaces from microfossils are filled by either ferroan calcite cement, pyrite/marcasite, micrite or green clay minerals. Both green clay minerals (berthierine, odinite or verdine facies) and glauconite indicate a shallow marine origin (Odin 1990; Ryan and Hillier 2002; Huggett 2013) prior to redeposition. Since aragonite,

the main component of other faecal pellets, is metastable and would be converted into calcite at shallow burial depths (e.g. Deik et al. 2019; Reuning et al. 2022), a recrystallization to dolomite is interpreted. However, as the partially dissolved pellets are crosscut by a ferroan calcite veins (Fig. 6a) and the intragranular porosity of the pellets remains uncemented, we interpret the formation of intragranular porosity to occur

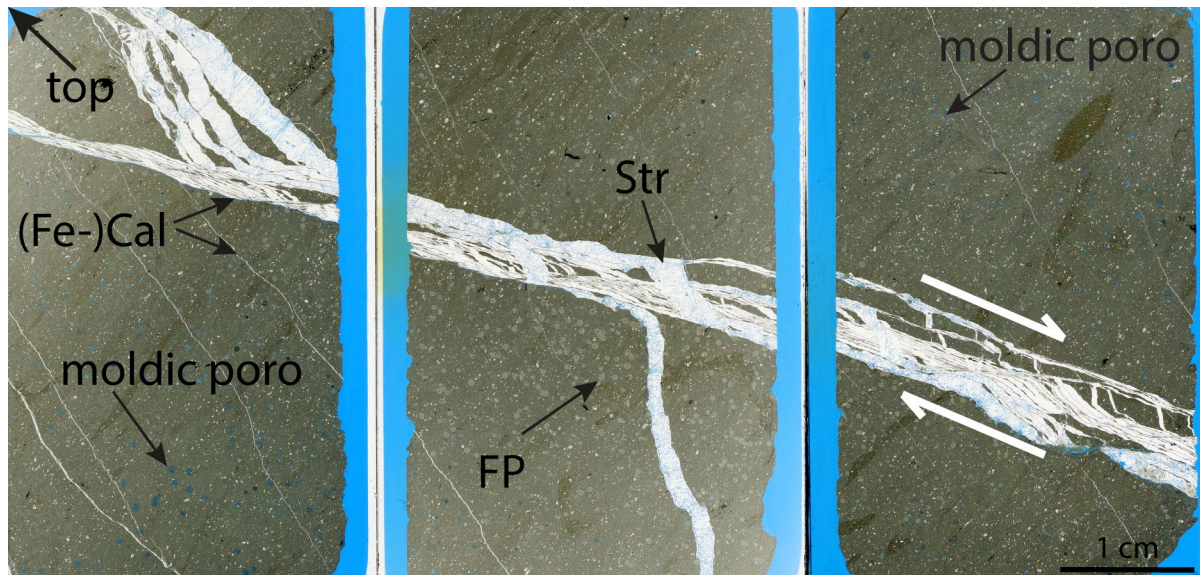


Fig. 8 Thin section scans (layer PHX10); the top of the layer is marked with an arrow on the upper left corner. Wider (ferroan) calcite veins precipitate syntaxially and include host rock fragments. Smaller (ferroan) calcite veins are parallel to each other. Faecal pellets are locally dissolved (moldic porosity, left side) or preserved (e.g.

in the centre). White arrows highlight normal fault displacement and associated extensional fracturing, resulting in a sheared (ferroan) calcite vein and vein reactivation with strontianite precipitation. (Fe-)Cal: (ferroan) calcite, moldic poro: moldic porosity, FP: faecal pellet, Str: strontianite

after fracturing and ferroan calcite vein formation, most likely during late diagenesis and exposure at the surface.

Paragenesis

Early diagenesis

Early diagenesis begins instantly after deposition and in conjunction with mechanical compaction of detrital components during overall shallow to intermediate burial (Fig. 13a). Based on regional reconstructions, the maximum burial depth likely did not exceed 1.5 km depth (Uffmann 2014). The compaction also allowed dehydration of the clay laminae, which additionally release elements (e.g. Fe^{2+} and Ca^{2+}) into solution, which is also described in the transformation of smectite to illite (Boles and Franks 1979). Furthermore, this initial compaction due to overburden resulted in the elliptical deformation and occasional fracturing of calcispheres close to clay laminae (Fig. 13c). The observed pyrite and marcasite as framboids in clay laminae and calcispheres likely incorporated iron liberated from clay mineral dehydration during initial compaction formed by bacterial sulphate reduction (BSR) in a shallow burial environment (Bernier 1970; Coleman 1985). The BSR onset is often spontaneous, if organic-rich sediments and lower oxygen penetration are present (Machel and Grobe 2001 and references therein). The main process of BSR is the microbial reduction of sulphate to hydrogen sulphide to form iron sulphide, aragonite dissolution, and an increase of alkalinity is the

consequence (Biehl et al. 2016; Deik et al. 2019 and references therein). This leads to precipitation of calcite cements (e.g. Friis 1995; Reuning et al. 2006; Deik et al. 2019) or dolomite and therefore to the lithification of the interpreted faecal pellets. However, incipient sulphate reduction can lead to carbonate dissolution due to a drop in pH (Reuning et al. 2022). The authors show that for specific cases a slightly higher concentration of organic matter allows an increased aragonite dissolution during sulphate reduction in the same depth, where dolomite cementation starts in a shallow burial environment (Reuning et al. 2022). The dolomitic composition of the pellets is supported by the pellets remaining unstained and showing a reddish luminescence in CL (Fig. 7f) (e.g. Götze 2012). Also, further microbial mediated processes such as iron reduction and methanogenesis could lead to diagenetic dolomite formation (Petrash et al. 2017, and references therein). Iron is a redox-sensitive element, and therefore the reduction by Fe(III)-respiring microorganisms leads to incorporation of iron in dolomite or newly formed carbonate overgrowths (Petrash et al. 2017, and references therein). The latter is depending on the occurrence of biologically produced sulphide anions, which could also lead to pyrite formation (Petrash et al. 2017, and references therein). As the calcispheres (both, deformed and intact) and also other fossils are filled with iron sulphides in the vicinity of clay laminae (Fig. 5a, d, f, g), a contemporaneous process of clay mineral dehydration and BSR (additional processes cannot be excluded) is interpreted. Furthermore, ferroan calcite precipitation is interpreted to postdate framboidal

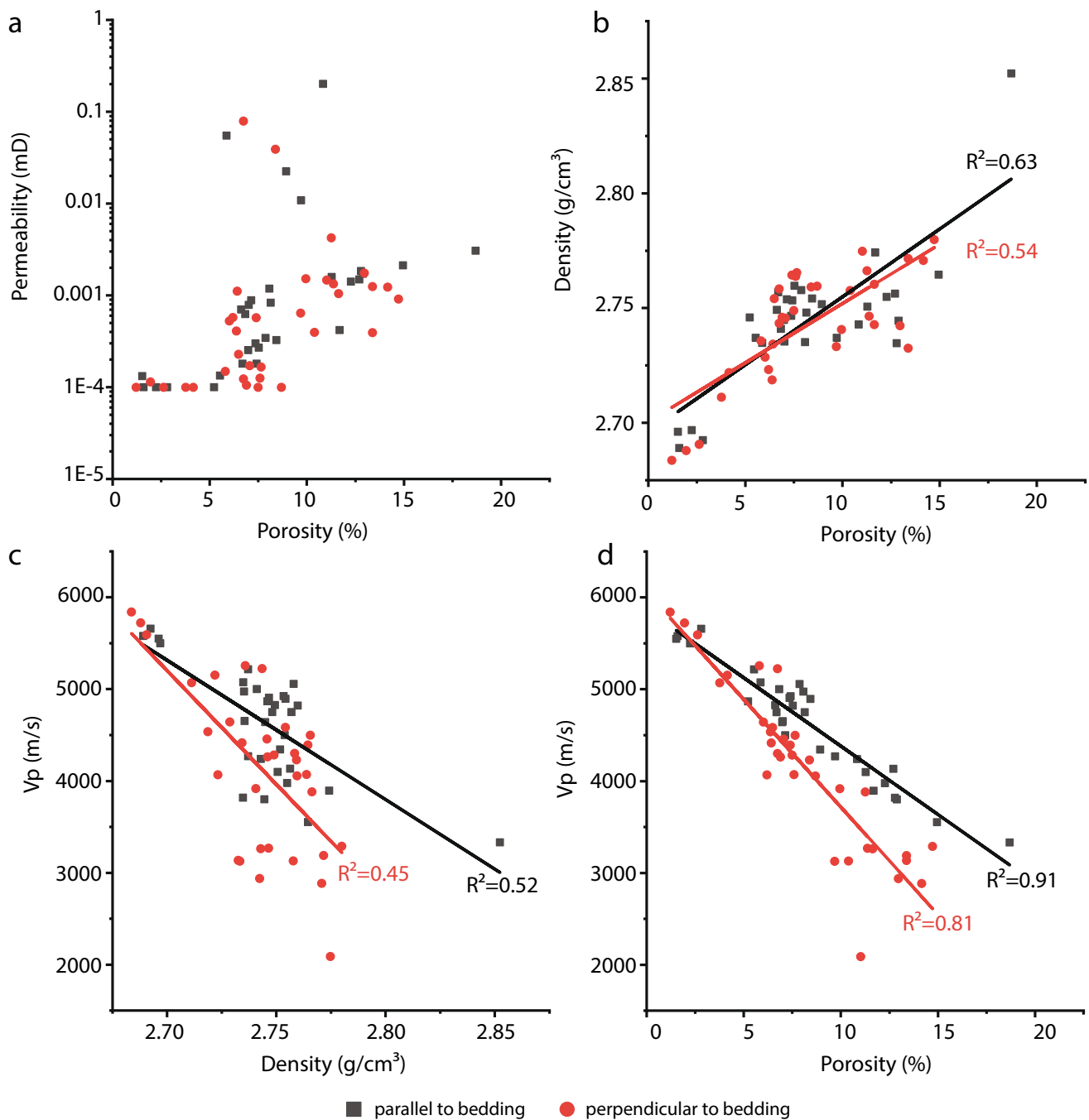


Fig. 9 Cross-plots of petrophysical data, **a** porosity (%) and permeability (mD), **b** porosity (%) and grain density (g/cm^3), **c** density (g/cm^3) and v_p (m/s), **d** porosity (%) and v_p (m/s)

pyrite/marcasite formation and compaction as it encases iron sulphides and fills intraparticle pores in deformed and undeformed calcispheres and foraminifera. The precipitation of ferroan calcite likely was enhanced by the release of Fe and Ca into solution by the clay mineral dehydration. The formation of ferroan carbonates by elemental uptake from intraformational claystones is also observed in sandstones (cf., Miocic et al. 2020), where Fe- and Mg-rich carbonates

are present in close proximity to clay layers. Also, the early burial release of Ca-ions by carbonate dissolution coupled to BSR could be feasible. However, the origin of early diagenetic calcite cements is debated as shown by Munnecke et al. (2023). Further mechanical compaction and fracturing of these initially hollow calcispheres (Voigt and Häntzschel 1964), which are now filled by ferroan calcite, is inhibited, while uncemented foraminifera or calcispheres would likely

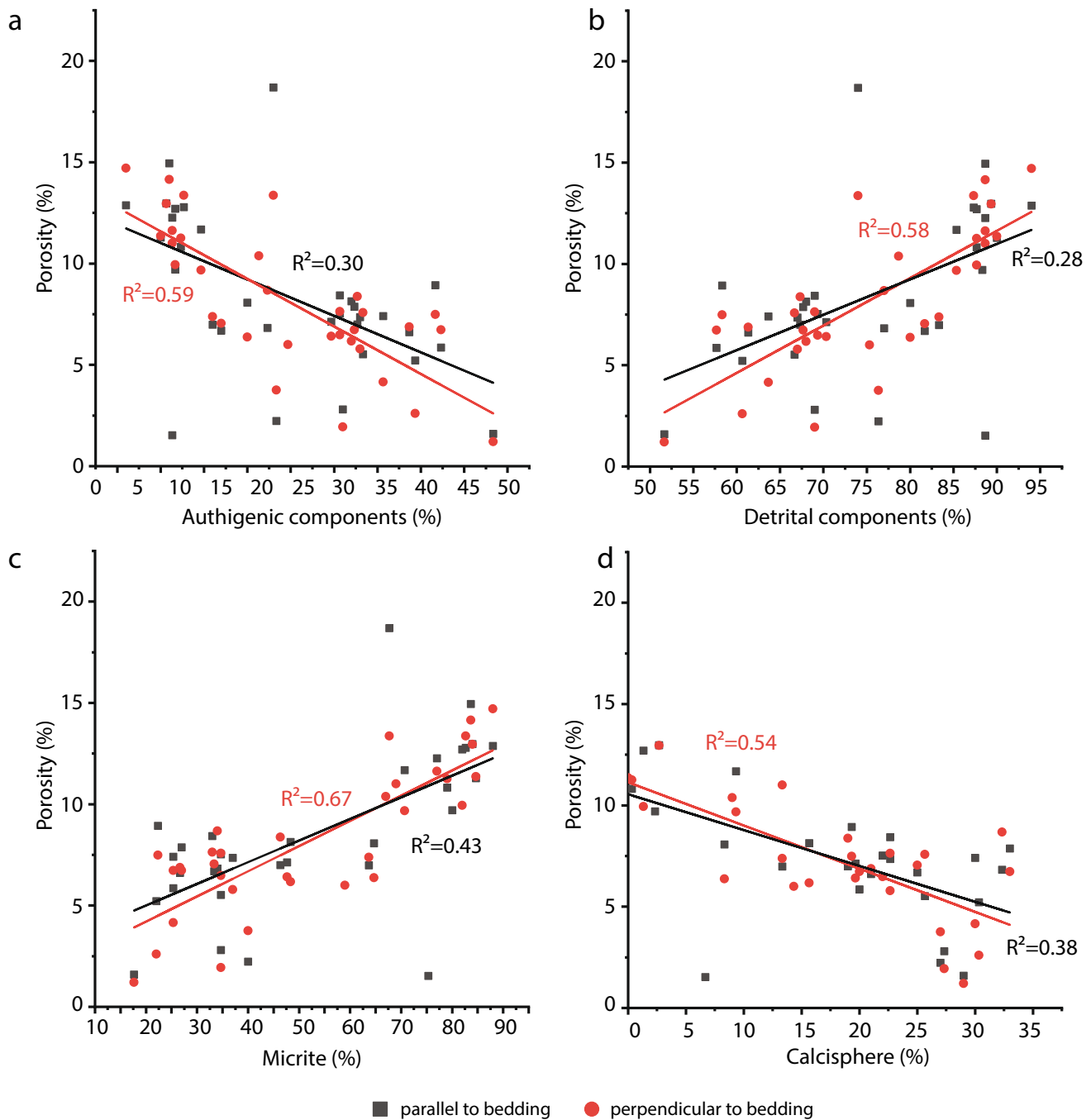


Fig. 10 Cross-plots of petrophysical and petrographic data, all given in (%), **a** authigenic components and He-porosity, **b** detrital components and He-porosity, **c** micrite and He-porosity and **d** calcspheres and He-porosity. The cross-plots indicate lower porosities in samples containing higher amounts of authigenic components and higher

porosities in samples containing higher amounts of detrital components. Since micrite and calcspheres are the main detrital parts, higher micrite content results in higher porosity, while samples containing higher amounts of calcspheres show lower porosities

crush under further mechanical stresses as derived from geomechanical laboratory tests on calcsphere-containing calcarenites (cf., Leuthold et al. 2021).

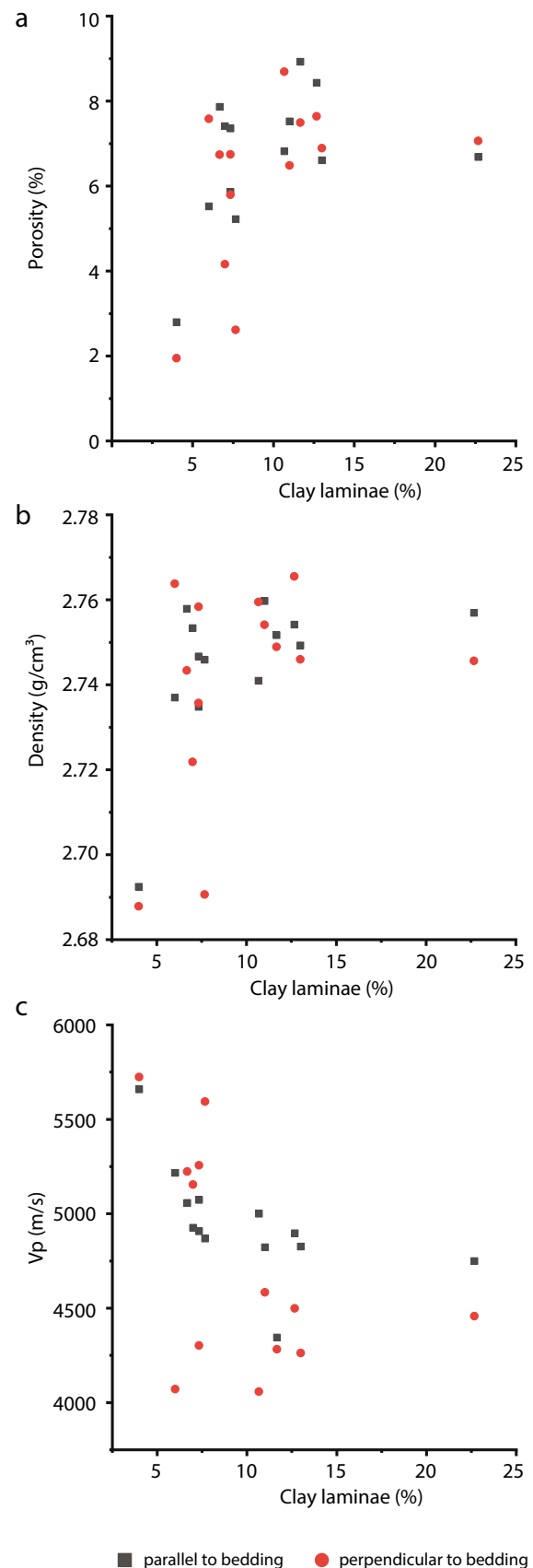
Late diagenesis

As (ferroan) calcite veins are following the outline of calcspheres filled by ferroan calcite (Fig. 5a, b), it is interpreted that they formed following the precipitation

Fig. 11 Cross-plot for He-porosity (%) and grain density (g/cm^3) with an amount of clay laminae (%) from point counting for samples containing at minimum 4% clay laminae, **a** higher porosity shows a slightly positive trend with higher amount of clay laminae, **b** higher amount of clay laminae (minimum 4%) shows a slightly positive trend with (b) density and a slightly negative trend with (c) v_p

of intraparticle ferroan calcite, as the hollow calcispheres would have likely fractured. Within these veins, cathodoluminescence indicates areas with higher amount of Fe or Mn, or REE, based on its luminescence (Fig. 7a) (Budd et al. 2000), and may indicate slight changes in fluid compositions during vein precipitation. Most of the ferroan calcite cements present a dull orange luminescence up to non-luminescence representing Fe enrichment relative to Mn (cf., Budd et al. 2000). The assessment of a variability in the Fe content during vein cement precipitation is also supported by carbonate staining showing calcitic (red) and ferroan calcitic (blue) zones in stained thin sections (Fig. 5a). As (ferroan) calcite in the wider composite veins often encases pyrite/marcasite in contact with the host rock, the initial precipitate in the fracture is interpreted to be pyrite/marcasite.

Fault controlled, late diagenetic fluid interactions can also precipitate iron sulphides (pyrite and marcasite) at the transition of the rock before the fractures are filled by (ferroan) calcite or strontianite (Grobe and Machel 2002). The elongate blocky (ferroan) calcite crystals with euhedral crystal terminations (Fig. 7b) indicate a large open fracture aperture in which crystal facets could form (Prajapati et al. 2018). The remaining fracture porosity was then filled by strontianite precipitating on the euhedral crystal facets (Fig. 7c, d) (cf., Giers 1958; Grobe and Machel 2002). Since the veins in general contain strontianite, (ferroan) calcite and sulphides, the paleo-fluid is interpreted as sodium chloride rich, probably influenced by Zechstein salts from Northern Germany (e.g. Harder 1964; Grobe and Machel 2002). Alternatively, the strontium content in mineralized deep water of the Ruhr area is up to 1530 mg Sr/l, which would be high enough for the formation of strontianite deposits in the central Münsterland (Dölling and Juch 2009, and references therein). These mineralized fluids may precipitate strontianite in contact with lower salinity formation waters in Cretaceous limestones, at lower pressures and temperatures of near-surface conditions (Dölling and Juch 2009, and references therein). Although no correlation between the regional concentrations of Sr in mineralized fluids from the Ruhr area and the presence of strontianite veins could be established, it is the more likely source for strontianite veins (Dölling and Juch 2009, and references therein). Earlier assumptions of lateral secretion from Upper Cretaceous limestones and marls (Kramm 1985) based on similar Sr isotope signatures have mostly been discarded, as the Sr content in these limestones does



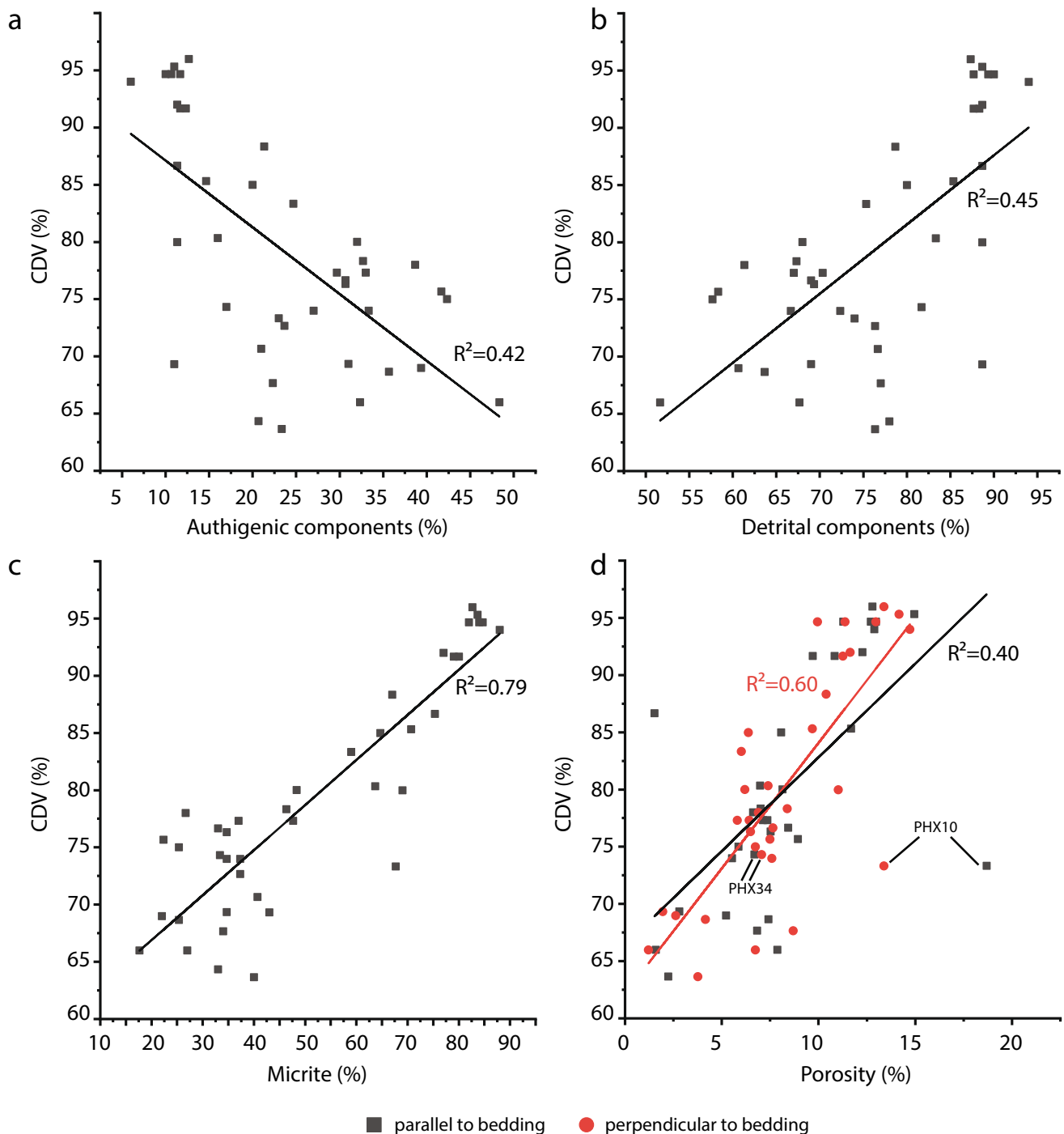


Fig. 12 Cross-plot for compactable depositional volume (CDV) with petrophysical and petrographic data, all given in (%). CDV versus **a** authigenic components, **b** detrital components, **c** micrite and **d** He-porosity. Higher CDV thus correlates negatively with the amount of authigenic components, but positively with detrital components, while micrite shows the best correlation. Higher CDV also correlates

with higher measured porosity. PHX10 marks the value for a sample with a CDV of 73.33%, containing no calcispheres but 67.67% micrite (porosity parallel and perpendicular to stratification of 18.69%, 13.38%) (Fig. 6). PHX34 marks a sample with a CDV of 74.33% containing 25% calcispheres and 33.33% micrite (porosity parallel and perpendicular to stratification of 6.69%, 7.07%) (Fig. 5a)

not change with increasing distance from the veins (Dölling and Juch 2009, and references therein). However, the formation of strontianite veins due to lateral secretion would also result in a more homogeneous occurrence of strontianite

veins in joints. In this study, as well as described by Bauch et al. (2003), strontianite veins are mostly restricted to NW–SE striking veins, and (subordinate) in NE–SW. As the strontianite veins are dominantly found in areas surrounding

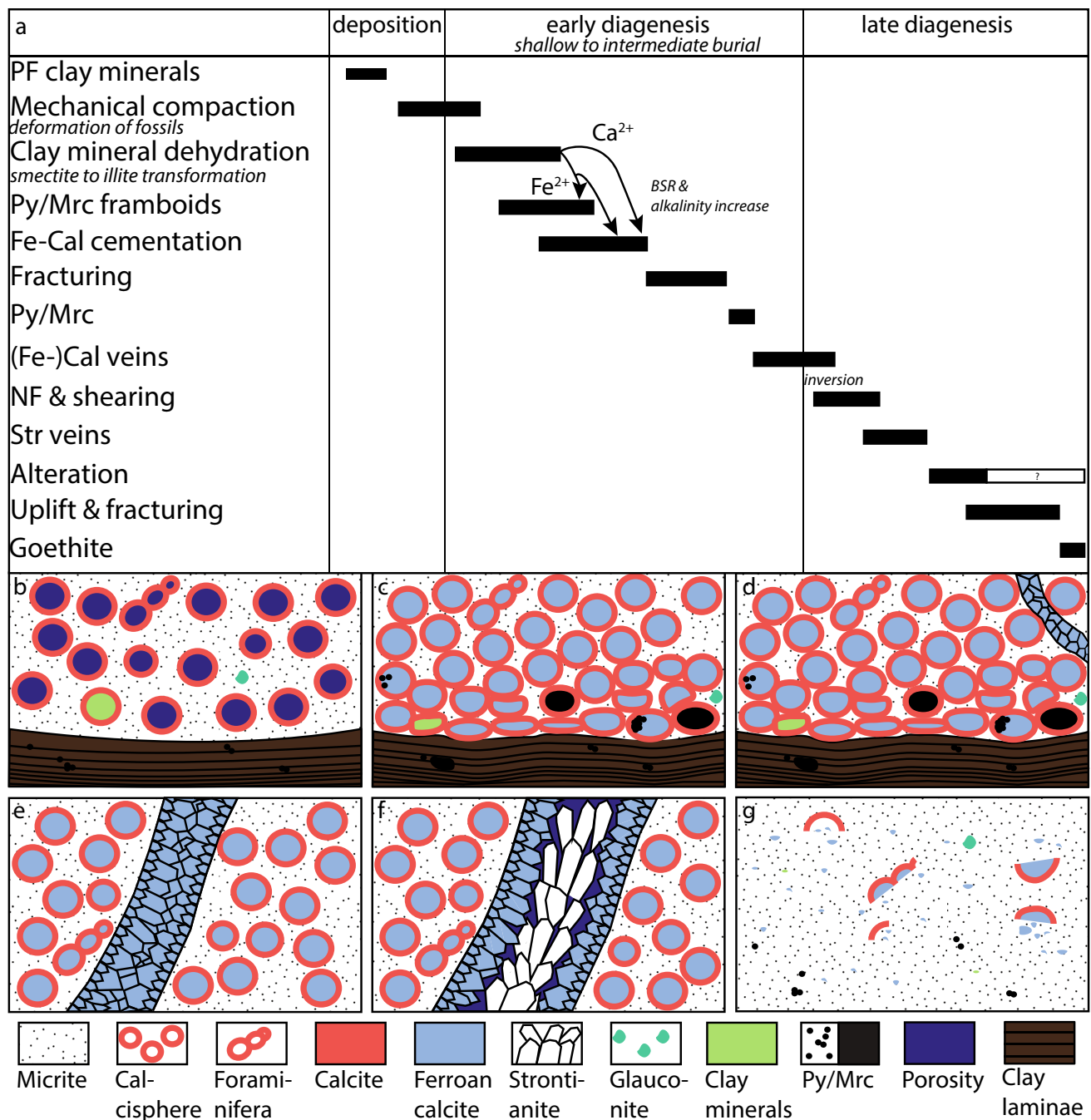


Fig. 13 Schematic illustration of the studied sections, **a** paragenetic sequence from deposition to late diagenesis of the studied carbonate rocks. Combination of rock and mineral composition, compaction and tectonic influence. **b** Calcspheres, foraminifera and other fossils, clay laminae and micrite are the main detrital components. Following (re-) deposition, calcspheres and other cavities within fossils are on occasion filled by green clay minerals and micrite or retain primary porosity. **c** Shallow to intermediate burial compaction due to overburden stress leads to grain rearrangement and deformation. The still hollow calcspheres are elliptically deformed and rarely broken, especially at the transition to ductile clay laminae, forming compaction bands. Simultaneously, BSR enables the formation of pyrite/marcasite framboids and ferroan calcite cements. **d** (Ferroan) calcite veins follow-

ing the outlines of cemented fossils are completely sealed. **e** Larger syntaxial euhedral (ferroan) calcite veins showing growth competition of elongate blocky crystals are also completely sealed. **f** Fault-controlled re-opening of (ferroan) calcite veins and late diagenetic fluid interaction lead to the formation of strontianite encasing euhedral calcite and ferroan calcite facets. **g** The upper part of the studied lithologies shows less fossils in general and a high micrite/clay content. Clay laminae are mostly missing. The fossils are broken and mainly ferroan calcite cement precipitates in intraparticle pores. Framboidal pyrite/marcasite is found within the clay-rich micritic matrix. PF: pore filling, BSR: bacterial sulphate reduction, Py/Mrc: pyrite/marcasite, Fe-Cal: ferroan calcite, (Fe-)Cal: (ferroan) calcite, NF: normal fault (or normal fault reactivation), Str: strontianite

faults within the Upper Cretaceous limestones of the region and mainly in NW–SE and only subordinately in NE–SW orientation, a relation with the Upper Cretaceous compressional event and inversion (e.g. Osning thrust) as a result of stress field change is interpreted (e.g. Drozdowski 1988; Kley and Voigt 2008; Dölling et al. 2017; Voigt et al. 2021). Fault-controlled movement of warm and saline strontium-rich formation fluids from fractured and deformed Palaeozoic bedrocks could be an additional source (Grobe and Machel 2002). As the host rock surrounding the sheared vein (Fig. 7e) also shows a purple luminescence of the micritic host rock, it is likely that in the vicinity to this sheared vein, the host rock was altered prior to (ferroan) calcite vein precipitation. Alternatively, a violet-blue luminescence in carbonates has previously been assigned to intrinsic lattice deformation in calcites (Toffolo et al. 2019). However, this cannot be linked to the shear displacement, as other host rock inclusions in the same sample still show an orange luminescence (Fig. 7b–d).

Shearing of the studied vein in sample PHX10 syndates the precipitation of (ferroan) calcite veins, as the displaced and cut host rock inclusions, which are stabilized by (ferroan) calcite veins, are again overgrown by calcite and ferroan calcite (Fig. 6b and 7). The shearing furthermore predates the precipitation of strontianite, as the (ferroan) calcite overgrowing cut host rock inclusions is encased in strontianite (Fig. 6c). As the partially dissolved faecal pellets are crosscut by narrow (ferroan) calcite veins (Fig. 6a), their dissolution is interpreted to postdate the latest phase of (shear) fracturing, (ferroan) calcite and strontianite precipitation. The most likely interpretation is dissolution due to exposure to meteoric water. However, the presence of faecal pellets is only restricted to this individual layer showing dissolution, resulting in moldic porosity, which enhances the porosity but not the permeability. As the fracture surfaces of the few observed open fractures contain brownish iron residue (Fig. 3a, b), most likely goethite stains, it is suggested that the open fractures formed near to the present-day surface in a humid, oxidizing climate (e.g. Burgess et al. 2016), likely during uplift and stress release.

Compaction and CDV

The average optical porosity derived from point counting is 0.32%. A lack of visible porosity, including macroporosity, may be caused by compaction. Macroporosity is only visible in samples containing dissolved pellets or within wider veins containing strontianite. Also, mechanical compaction is indicated by well-defined laminae interpreted as compaction bands, where elliptically deformed calcispheres and clay laminae are in contact. Initial mechanical compaction after (re)deposition causes grain rearrangement, while ductile clay laminae form boundaries, where the calcispheres

deformed elliptically and even break. The average vertical compaction is 38.5%, but since the determination of compaction by Fry (1979) is in this case related to calcispheres at the transition to clay laminae, no overall correlation could be done, since not every thin section contains calcispheres and clay laminae. The elliptical deformation of calcispheres in the Münsterland Cretaceous Basin was already recognized by Giers (1958), but not quantified. As the combination of compacted calcispheres and clay laminae forms compaction bands parallel to bedding, direction-dependent hydraulic properties, e.g. permeability perpendicular to the compaction band, are decreased by on avg. 0.4 orders of magnitude. This effect is also observed for compaction bands formed during geomechanical lab experiments (c.f. Stanchits et al. 2009; Baud et al. 2012; Leuthold et al. 2021). Similar to the use of palynomorphs (cf. Pliocene of Great Bahama Bank or Silurian of Gotland, Westphal and Munneke 1997) as a compaction indicator in fine-grained carbonates, calcispheres and also other intraporosity bearing fossils can record localized compaction. To further assess the impact of compaction based on petrographic parameters, similar to the IGV calculations in sandstones (Houseknecht 1987; Paxton et al. 2002), the concept of the ‘compactable depositional volume’ was evaluated. As both compaction and cementation influence the volume and porosity loss during diagenesis and one process may limit the other, we chose the CDV to assess controlling factors on volume and porosity. Samples with higher measured He-porosity show higher CDV, which means that depositional porosity and volume is retained and can be assessed using the CDV. However, a higher proportion of authigenic cements shows lower CDV and porosity values (Fig. 10a and 12a), indicating that the cementation reduces porosity but does not effectively inhibit compaction, supporting the assessment that the cements formed after initial compaction. Furthermore, the CDV shows a positive correlation with detrital minerals (Fig. 12b). This is related to the large proportion of micritic matrix, which preserves microporosity (Zhang and Lu 2019) which enhances the CDV. As micrite has a high intercrystalline porosity at deposition of up to ~80% (Bathurst 1970; Shinn et al. 1977; Moshier 1989; Goldhammer 1997; Zhang and Lu 2019), it is included in this assessment, just as depositional clay mineral matrix is included in IGV assessments in sandstones (Paxton et al. 2002). After Lee et al. (2021), the initial porosity of Miocene to Holocene wackestones of the west coast of Australia starts at ~60%. Although the composition or texture of some samples, as well as the measured He-porosity varies, the CDV can show similar values, as shown in Fig. 12d. The sample PHX10 (Fig. 7b–f) shows a CDV of 73.33% and a porosity of 18.69% parallel to the stratification and 13.38% perpendicular to the stratification, whereas the sample PHX34 (Fig. 7a, 5a) shows a CDV of 74.33%, but a porosity of 6.69% parallel to the

stratification and 7.07% perpendicular to the stratification. The sample PHX10 is composed mostly of micrite (67.67%) and no calcispheres, whereas the sample PHX34 contains 25% calcispheres and 33.33% micrite. High CDV values (e.g. 96% in sample PHX05) are an effect of overrepresentation of micrite. The same effect, however, can be observed in IGV calculations of sandstone samples rich in depositional clay minerals (c.f. Paxton et al. 2002). However, the optical porosity in the thin sections is determined by point counting and does not include microporosity in micrite and clay minerals or clay minerals in laminae because of the limited magnification of the microscope. Also, just as with depositional clay mineral matrix in sandstones and their effect on compaction (i.e. IGV in Paxton et al. 2002), the initial microporosity of micrite is not included in the calculation of the CDV. In contrast, sandstones do not necessarily contain grains with primary intraparticle porosity apart from fossils, which can be reduced by compaction. As the primary porosity in carbonate rocks is influenced by pre-depositional and depositional processes (Choquette and Pray 1970), both have to be considered to analyse the CDV. If applicable in similar lithologies, the CDV may be a suitable indicator for post-depositional compaction in limestones containing components or fossils with intraparticle porosity and may capture the compactional effect on reservoir properties. The CDV should be a basis to compare samples within the same stratigraphy and to relate the effect of compaction on petrophysical parameters as measured porosity and permeability. Also, as described by Lee et al. (2021), the compaction behaviour of carbonate rocks varies, as well as the early stage of porosity.

Reservoir quality controlling factors

The reservoir quality controlling factors for the analysed lithology are (1) mechanical compaction, which leads to grain rearrangement, (micro)porosity loss and formation of compaction bands at ductile clay laminae boundaries; (2) cementation of former pore spaces with mainly ferroan calcite and (3) vein formation of (ferroan) calcite and strontianite, overall reducing the porosity and permeability. The subordinate dissolution of faecal pellets slightly enhances porosity but not permeability, since the moldic pores are not connected (Figs. 6b, 7f, 8). Also, particle sizes influence porosity, as micrite and clay laminae still contain microporosity, whereas calcispheres are fully cemented. Tests are most likely not cemented, which contributes to the microporosity (e.g. Abouelresh and Mahmoud 2022). However, a higher amount of calcispheres causes lower He-porosities and higher v_p values, likely related to larger volumes of ferroan calcite cements precipitating in the intraparticle pores. Also, compaction and a decrease of porosity enhance v_p values (e.g. Anselmetti and Eberli 1993). The recorded sonic matrix

compressional velocity range is typical for limestones with an average porosity of 5–20% (Rider and Kennedy 2011). Slightly better correlating v_p and porosity values parallel to bedding are related to clay laminae and compacted calcispheres or calcisphere clasts aligned to the bedding. Also, the mineralogical composition as well as fabric can influence the sonic matrix compressional velocity (Kenter et al. 2007). In this study, the amount of clay laminae in samples with a minimum content of 4% shows a slightly negative correlation with v_p (Fig. 11c). Another influencing factor are pore types, as carbonate rocks can include various pore sizes and types (e.g. Weger et al. 2009). Positive deviations of a porosity–velocity trend and therefore higher velocity values can be caused by the pore type and the depositional and diagenetic overprint, which is shown by Anselmetti and Eberli (1999). However, macroporosity within the thin sections in this study is poor, except for layer PHX10 due to dissolution processes. Porosity and permeability values are generally low and show no log-linear correlation (Fig. 9a). For samples drilled parallel to the stratification, higher grain density correlates with higher He-porosity (Fig. 9b), which also correlates with higher amounts of clay laminae (Fig. 11a, b) and the presence of compaction bands in samples containing clay laminae (Fig. 5d).

Micrite, clay laminae and fossil tests contain microporosity, which is not visible in the thin sections using transmitted light microscopy, but can influence petrophysical properties, which is known from clays in sandstones (e.g. Nadeau and Hurst 1991). In general, the influence of micrite and clay laminae depends on their texture, pore space geometry and sizes (e.g. Volery et al. 2010; Deville de Periere et al. 2011; Regnet et al. 2015; Smodej et al. 2019). Samples containing more than 4% clay laminae show a slightly positive trend with higher porosity and grain density (Fig. 11a, b). Plugs drilled parallel to the stratification are of factor 1.4 higher for the maximum permeability than that of samples drilled perpendicularly to the stratification. This is largely related to the anisotropy related to compacted calcispheres and clay laminae (Fig. 5d), since clay layers and compaction bands are known to act as fluid flow barriers (c.f. Kayser 2006). But in average, the permeability is in the same order. In addition, mechanical compaction decreases porosity and permeability in general (e.g. Halley and Schmoker 1983; David et al. 2001; Croizé et al. 2013), since grain rearrangement and calcisphere deformation reduce the inter- and intragranular pore space and pore throat sizes. Smaller amounts of calcispheres in higher strata of the lithological column can thus be related to slightly higher permeabilities, which is interpreted to be related to a higher amount of micrite (Fig. 2) and a lower degree of compaction. As the lower measurement limit of the permeameter is 0.0001 mD, the permeability of samples given as 0.0001 mD will likely be lower, enhancing the sealing potential of the host rock.

The effect of diagenesis in the studied samples reduces the reservoir quality in general, since carbonate cements filled former pore spaces and fractures. Large-scale, near-surface fluid flow is thus likely restricted to faults and fractures (e.g. Grobe and Machel 2002), as also observed in injection tests in the area of Münster (Mohrdeick 1996). Veins are mostly sealed with (ferroan) calcite, rarely strontianite or both, and only a few open fractures were observed in the quarry. However, they may also be an effect of carbonate vein dissolution during weathering and quarry operation or an effect of stress release during uplift (e.g. Wyrick and Borchers 1981). Goethite was formed likely by the alteration of pyrite in the host rock and stained the surface (cf., Burgess et al. 2016). Otherwise, the fractures would have likely been sealed by (ferroan) calcite or strontianite, as documented for the veins, and do not contribute to fluid flow in the subsurface. As the studied samples originate directly from and further away from the fault zone (Fig. 3c), and petrophysical data do not vary distinctly around the fault (supplementary material), the fault zone is interpreted to not influence porosity and permeability in the host rock. Dissolution is limited to one layer (PHX10), which increases porosity, but not the permeability. Due to the presence of (ferroan) calcite and strontianite as vein precipitates, the reservoir quality is low and the studied lithologies are therefore tight. Therefore, the studied lithologies in the Central Münsterland Cretaceous Basin, overlying the northernmost extent of subsurface coal mining, are likely acting as sealing lithologies. Although vertical variations in the composition of limestones and marly shales and thicknesses are known, the lithologies show a continuous lateral extent on up to 150 km² (Giers 1958). Only at the transition to the basin border, inhomogeneities can be expected (Giers 1958). However, the studied lithologies are partially overlying the northern extend of former coal-mining districts, and thus may not be representative for the whole coal-mining district. The facies with its deposited sediments will vary towards the south (c.f. Figure 1a).

Conclusions

The study of Upper Campanian limestones (Beckum Member) illustrates the impact of early and late diagenetic processes in former high porosity, mostly detrital rocks. Low matrix porosity (1.0 to 18.7%) and permeability (<0.0001 to 0.2 mD) is related to mechanical compaction, resulting in compaction bands and early cementation of former pore spaces with mainly ferroan calcite. Only marginal dissolution of faecal pellets slightly improves porosity but not permeability, which is seen only in one layer. Fractures are cemented and sealed by (ferroan) calcite and mostly preferred NW–SE orientated strontianite, due to the Late Cretaceous inversion and reactivation of fault systems. The

precipitation of (ferroan) calcite and strontianite veins further diminished large-scale fluid pathways. The rocks around the studied fault do not show different petrophysical properties or diagenetic alteration as surrounding rocks in the quarry. Open and brownish coated fractures are most likely uplifted related. Due to the low matrix permeability below 0.2 mD, lithologies can be considered as seals. This also indicates that a geothermal utilization of this formation at depth may be limited. Overall, the up to 25-m-thick Beckum Member limestone and marly shale alternation from the Upper Cretaceous acts as a regional seal, if not faulted with associated fractured damage zones. Only open fractures and faults, if present in the subsurface, could enhance fluid pathways. Therefore, fault-related fluid flow may have been limited.

The compactable depositional volume (CDV) for carbonate rocks, derived from petrographic thin section analyses, may be a useful tool to assess the timing of cementation in relation to compaction if components with intraparticle porosity are present and to assess the effect of compactional volume loss on reservoir properties. The effect of overrepresentation by micrite and therefore high CDV values is comparable to the effect from IGV calculations of sandstone samples rich in depositional clay minerals.

Supplementary Information The online version contains supplementary material available at <https://doi.org/10.1007/s00531-024-02411-z>.

Acknowledgements Phoenix Zementwerke Krogbeumker GmbH & Co. KG in Beckum (Germany), especially Patrick Pottmeier & Wolfgang Schnieders, are thankfully acknowledged for the opportunity of field work and sample collection in March 2022. Martin von Dollen is thanked for preparing the thin sections at the Institute of Structural Geology and Tectonics, Institute of Applied Geosciences (KIT), and Felix Allgaier for providing the drone imagery. Funding for field work is acknowledged by the Federal Ministry of Education and Research (BMBF) (grant no. 03G0893A).

Funding Open Access funding enabled and organized by Projekt DEAL.

Data availability All available data is provided as an electronic supplementary material file.

Declarations

Conflict of interest The authors declare that they have no competing interests.

Open Access This article is licensed under a Creative Commons Attribution 4.0 International License, which permits use, sharing, adaptation, distribution and reproduction in any medium or format, as long as you give appropriate credit to the original author(s) and the source, provide a link to the Creative Commons licence, and indicate if changes were made. The images or other third party material in this article are included in the article's Creative Commons licence, unless indicated otherwise in a credit line to the material. If material is not included in the article's Creative Commons licence and your intended use is not permitted by statutory regulation or exceeds the permitted use, you will

need to obtain permission directly from the copyright holder. To view a copy of this licence, visit <http://creativecommons.org/licenses/by/4.0/>.

References

- Abouelresh M, Mahmoud M (2022) Petrographic characterization of microporosity in the organic-rich carbonate Hanifa Formation, Jafurah Basin, Saudi Arabia. 3540–3542. <https://doi.org/10.1190/image2022-3745573.1>
- Abuamarah BA, Nabawy BS (2021) A proposed classification for the reservoir quality assessment of hydrocarbon-bearing sandstone and carbonate reservoirs: a correlative study based on different assessment petrophysical procedures. *J Natl Gas Scie Eng* 88:103807. <https://doi.org/10.1016/j.jngse.2021.103807>
- Ahr M (2008) Geology of carbonate reservoirs: the identification, description, and characterization of hydrocarbon reservoirs in carbonate rocks: pp 277
- Amthor JE, Mountjoy EW, Machel HG (1994) Regional-scale porosity and permeability variations in Upper Devonian Leduc buildups: Implications for reservoir development and prediction in carbonates. *AAPG Bull* 78:1541–1559. <https://doi.org/10.1306/A25FF215-171B-11D7-8645000102C1865D>
- Anselmetti FS, Eberli GP (1993) Controls on sonic velocity in carbonates. *Pure Appl Geophys* 141(2):287–323. <https://doi.org/10.1007/BF00998333>
- Anselmetti F, Eberli G (1999) The velocity-deviation log: a tool to predict pore type and permeability trends in carbonate drill holes from sonic and porosity or density logs. *AAPG Bull* 83:450–466
- Armitage PJ, Worden RH, Faulkner DR, Aplin AC, Butcher AR, Espie AA (2013) Mercia mudstone formation caprock to carbon capture and storage sites: petrology and petrophysical characteristics. *J Geol Soc* 170(1):119–132. <https://doi.org/10.1144/jgs2012-049>
- Arnold H, Bode H, Wortmann H, Karrenberg H, Teichmüller R (1960) Erläuterungen zu Blatt Münster C 4310, Übersichtskarte von Nordrhein-Westfalen 1:100 000. Krefeld, Geologisches Landesamt Nordrhein-Westfalen: 24–34
- Bathurst RGC (1970) Problems of lithification in carbonate muds. *Proc Geol Assoc* 81(3):429–440. [https://doi.org/10.1016/S0016-7878\(70\)80005-0](https://doi.org/10.1016/S0016-7878(70)80005-0)
- Bauch E, Hecht C, Lempp C, Wrede V (2003) Transpressive Tektonik im Campan von Beckum, Zentrales Münsterland, Nordrhein-Westfalen. *Script Arbeitsergebnisse Aus Dem Geologischen Dienst Nordrhein-Westfalen* 10:5–17
- Baud P, Meredith P, Townend E (2012) Permeability evolution during triaxial compaction of an anisotropic porous sandstone. *J Geophys Res Solid Earth* 117(B5):B05203. <https://doi.org/10.1029/2012JB009176>
- Becker I, Wüstefeld P, Koehler B, Felder M, Hilgers C (2017) Porosity and permeability variations in a tight gas sandstone reservoir analog, Westphalian D, Lower Saxony Basin, NW Germany: influence of depositional setting and diagenesis. *J Petrol Geol* 40(4):363–389. <https://doi.org/10.1111/jpg.12685>
- Berner RA (1970) Sedimentary pyrite formation. *Am J Sci* 268(1):1–23. <https://doi.org/10.2475/ajs.268.1.1>
- Biehl BC, Reuning L, Schoenherr J, Lüders V, Kukla PA (2016) Impacts of hydrothermal dolomitization and thermochemical sulfate reduction on secondary porosity creation in deeply buried carbonates: a case study from the Lower Saxony Basin, northwest Germany. *AAPG Bull* 100(4):597–621. <https://doi.org/10.1306/01141615055>
- Boles JR, Franks SG (1979) Clay diagenesis in Wilcox sandstones of Southwest Texas; implications of smectite diagenesis on sandstone cementation. *J Sediment Res* 49(1):55–70. <https://doi.org/10.1306/212f76bc-2b24-11d7-8648000102c1865d>
- Bouma AH (1964) Turbidites. In: Bouma AH, Brouwer A (eds) *Developments in sedimentology*, 3rd edn. Elsevier, London, pp 247–256
- Bouma AH (2004) Key controls on the characteristics of turbidite systems. *Geol Soc Lon Spec Publ* 222(1):9–22. <https://doi.org/10.1144/GSL.SP.2004.222.01.02>
- Budd DA, Hammes U, Ward WB (2000) Cathodoluminescence in calcite cements new insights on Pb and Zn sensitizing, Mn activation, and Fe quenching at low trace-element concentrations. *J Sediment Res* 70:217–226. <https://doi.org/10.1306/2DC4090C-0E47-11D7-8643000102C1865D>
- Burgess DT, Kettler RM, Loope DB (2016) The geologic context of wonderstone: a complex, outcrop-scaled pattern of iron-oxide cement. *J Sediment Res* 86:498–511. <https://doi.org/10.2110/jsr.2016.35>
- Busch B, Becker I, Koehler B, Adelmann D, Hilgers C (2019) Porosity evolution of two Upper Carboniferous tight-gas-fluvial sandstone reservoirs: impact of fractures and total cement volumes on reservoir quality. *Mar Pet Geol* 100:376–390. <https://doi.org/10.1016/j.marpetgeo.2018.10.051>
- Choquette PW, Pray LC (1970) Geologic nomenclature and classification of porosity in sedimentary carbonates. *AAPG Bull* 54(2):207–250. <https://doi.org/10.1306/5d25c98b-16c1-11d7-8645000102c1865d>
- Coffa AA, O'Mara MJ, McLaren C, Thompson DL, Karakatsanis J, Hall M, Stilwell J (2015) Enhancing oil and gas production in carbonate turbidite fields by the study of high-resolution biostratigraphy, facies and fracture variability: an example from the NW Palawan Basin of the Philippines. *SEG Global Meet Abstr*. <https://doi.org/10.1190/ice2015-2213451>
- Coldewey WG, Wesche D (2017) Hydrogeologische und gesteinsphysikalische Eigenschaften der Emscher-Formation im Hinblick auf den Steinkohlenbergbau des Ruhrgebietes. *Grundwasser* 22(3):175–183. <https://doi.org/10.1007/s00767-017-0365-0>
- Coleman ML (1985) Geochemistry of diagenetic, non-silicate minerals: kinetic considerations. *Philos Trans R Soc Lond Series a, Math Phys Sci* 315:39–56. <https://doi.org/10.1098/rsta.1985.0028>
- Croizé D, Renard F, Gratier J-P (2013) Compaction and porosity reduction in carbonates: a review of observations, theory, and experiments. *Adv Geophys* 54:181–238. <https://doi.org/10.1016/B978-0-12-380940-7.00003-2>
- David C, Menendez B, Zhu W, Wong TF (2001) Mechanical compaction, microstructures and permeability evolution in sandstones. *Phys Chem Earth Part A* 26(1):45–51. [https://doi.org/10.1016/S1464-1895\(01\)00021-7](https://doi.org/10.1016/S1464-1895(01)00021-7)
- Deik H, Reuning L, Petrick B, Takayanagi H (2019) Hardened faecal pellets as a significant component in deep water, subtropical marine environments. *Deposit Record* 5(2):348–361. <https://doi.org/10.1002/dep2.64>
- Deville de Periere M, Durlot C, Vennin E, Lambert L, Bourillot R, Caline B, Poli E (2011) Morphometry of micrite particles in cretaceous microporous limestones of the Middle East: Influence on reservoir properties. *Mar Pet Geol* 28(9):1727–1750. <https://doi.org/10.1016/j.marpetgeo.2011.05.002>
- Dickson JAD (1965) A modified staining technique for carbonates in thin section. *Nature* 205(4971):587. <https://doi.org/10.1038/205587a0>
- Dölling M, Juch D (2009) Strukturgeologische Modellvorstellungen zum Kreide-Deckgebirge im: zentralen Münsterland in Zwei Beiträge zur Geologie des zentralen und des südlichen

- Münsterlandes. Script Online Geowissenschaftliche Arbeitsergebnisse Aus Nordrhein-Westfalen 18:5–27
- Dölling B, Dölling M, Hiss M, Berensmeier M, Püttmann T (2017) Upper Cretaceous shallow-marine deposits of the southwestern Münsterland (northwest Germany) influenced by synsedimentary tectonics. *Cretac Res* 87:261–276. <https://doi.org/10.1016/j.cretres.2017.05.002>
- Dott RH (1963) Dynamics of subaqueous gravity depositional processes. *AAPG Bull* 47(1):104–128. <https://doi.org/10.1306/bc743973-16be-11d7-8645000102c1865d>
- Drozdowski G (1988) Die Wurzel der Osning-Überschiebung und der Mechanismus Herzynischer Inversionsstörungen in Mitteleuropa. *Geologische Rundschau*. *Geol Rundsch* 77(1):127–141. <https://doi.org/10.1007/BF01848680>
- Drozdowski G, Dölling M (2018) Elemente der Osning-Störungszone (NW-Deutschland) - Leitstrukturen einer Blattverschiebungszone. Script Online - Geowissenschaftliche Arbeitsergebnisse Aus Nordrhein-Westfalen 7:5–9
- Dunham RJ (1962) Classification of carbonate rocks according to depositional texture. In: Ham WE (ed) Classification of carbonate rocks a: symposium, 1st edn. AAPG, pp 108–121
- Ehrenberg SN (2006) Porosity destruction in carbonate platforms. *J Pet Geol* 29(1):41–52. <https://doi.org/10.1111/j.1747-5457.2006.00041.x>
- Ehrenberg SN, Nadeau PH (2005) Sandstone vs carbonate petroleum reservoirs: a global perspective on porosity-depth and porosity-permeability relationships. *AAPG Bull* 89(4):435–445. <https://doi.org/10.1306/11230404071>
- Ehrenberg SN, Eberli GP, Keramati M, Moallemi SA (2006) Porosity-permeability relationships in interlayered limestone-dolostone reservoirs. *AAPG Bull* 90(1):91–114. <https://doi.org/10.1306/08100505087>
- Erbacher J, Bornemann A, Petrizzo MR, Huck S (2020) Chemostratigraphy and stratigraphic distribution of keeled planktonic foraminifera in the Cenomanian of the North German Basin. *Zeitschrift der Deutschen Gesellschaft für Geowissenschaften* 171:149–161. <https://doi.org/10.1127/zdgg/2020/0211>
- Folk RL (1959) Practical petrographic classification of limestones I. *AAPG Bull* 43(1):1–38. <https://doi.org/10.1306/0bda5c36-16bd-11d7-8645000102c1865d>
- Folk RL (1974) The natural history of crystalline calcium carbonate; effect of magnesium content and salinity. *J Sediment Res* 44(1):40–53. <https://doi.org/10.1306/74d72973-2b21-11d7-8648000102c1865d>
- Friis H (1995) The role of faecal pellets in deposition of marine muddy sediments examples from the Danish Tertiary. *Bull Geol Soc Den* 42:68–73. <https://doi.org/10.37570/bgsgd-1995-42-07>
- Fry N (1979) Random point distributions and strain measurement in rocks. *Tectonophysics* 60(1):89–105. [https://doi.org/10.1016/0040-1951\(79\)90135-5](https://doi.org/10.1016/0040-1951(79)90135-5)
- Geologischer Dienst NRW (2020) Grubenwasser – Geodaten für den Nachbergbau https://www.gd.nrw.de/gw_be_grundwasserschutz-nachbergbau.htm. Accessed 20. January 2024
- Giers R (1958) Die Mukronatenkreide im östlichen Münsterland: Fazies, Stratigraphie und Lagerung. Hannover, Beihefte Zum Geologischen Jahrbuch, Heft 34:1–148
- Goldhammer RK (1997) Compaction and decompaction algorithms for sedimentary carbonates. *J Sediment Res* 67(1):26–35. <https://doi.org/10.1306/d42684e1-2b26-11d7-8648000102c1865d>
- Götze J (2012) Application of cathodoluminescence microscopy and spectroscopy in geosciences. *Microsc Microanal* 18(6):1270–1284. <https://doi.org/10.1017/S1431927612001122>
- Grobe M, Machel HG (2002) Saline groundwater in the Münsterland Cretaceous Basin, Germany: clues to its origin and evolution. *Mar Pet Geol* 19:307–322. [https://doi.org/10.1016/S0264-8172\(02\)00019-3](https://doi.org/10.1016/S0264-8172(02)00019-3)
- Halley RB, Schmoker JW (1983) High porosity Cenozoic carbonate rocks of south Florida: Progressive loss of porosity with depth. *Am Assoc Petrole Geol Bull* 67.
- Harder H (1964) Geochemische Untersuchungen zur Genese der Strontianitlagerstätten des Münsterlandes. *Beiträge zur Mineralogie und Petrographie* 10(2):198–215. <https://doi.org/10.1007/BF02652615>
- Healy D, Rizzo RE, Cornwell DG, Farrell NJC, Watkins H, Timms NE, Gomez-Rivas E, Smith M (2017) FracPaQ: A MATLAB™ toolbox for the quantification of fracture patterns. *J Struct Geol* 95:1–16. <https://doi.org/10.1016/j.jsg.2016.12.003>
- Hiss M (1995) Kreide. (ed) *Geologie im Münsterland*, Hans Dieter, H., Drozdowski, G., Krefeld, pp 41–65
- Hiss M, Mutterlose J (2010) Field trip E6: Cretaceous geosites of the eastern Ruhr Area and the southern Münsterland. *Schriftenreihe der Deutschen Gesellschaft für Geowissenschaften* 66:168–183. <https://doi.org/10.1127/sdgg/66/2010/168>
- Houseknecht DW (1987) Assessing the relative importance of compaction processes and cementation to reduction of porosity in sandstones. *AAPG Bull* 71(6):633–642. <https://doi.org/10.1306/9488787f-1704-11d7-8645000102c1865d>
- Huggett JM (2013) Minerals: glauconites and green clays. Elsevier. <https://doi.org/10.1016/b978-0-12-409548-9.02893-1>
- Janetschke N, Wilmsen M (2013) Magnetische Suszeptibilität als stratigraphisches Werkzeug – eine unterstützende Methode zur klassischen Profilaufnahme (Fallstudie: norddeutsche Oberkreide von Halle/Westfalen). *Geol Sax J Central Euro Geol* 59:149–163
- Kaplan U (2004) Neue Beobachtungen zu den Stromberg-Schichten, Untercampan, Oberkreide, südöstliches Münsterland. *Geol Paläont Westf* 62:71–110
- Kaplan U, Kennedy W, Ernst G (1996) Stratigraphie und Ammonitenfaunen des Campan im südöstlichen Münsterland. *Geologie und Paläontologie in Westfalen* 43.
- Kappel J (2002) Ichnofossilien im Campanium des südöstlichen Münsterlandes. Doctoral dissertation, Westfälische Wilhelms-Universität Münster
- Kayser A (2006) Herkunft, Auftreten und Visualisierung von Permeabilitätsbarrieren in einer Gaslagerstätte in Sandsteinen des Rotliegenden (Südliches Permbecken, Deutschland): Bedeutung für Diagenese. Philipps-Universität Marburg, Fluidfluß und Produktion.
- Kenter JAM, Braaksma H, Verwer K, van Lanen XMT (2007) Acoustic behavior of sedimentary rocks: geologic properties versus Poisson's ratios. *Lead Edge* 26(4):436–444. <https://doi.org/10.1190/1.2723206>
- Kley J, Voigt T (2008) Late Cretaceous intraplate thrusting in central Europe: Effect of Africa-Iberia-Europe convergence, not Alpine collision. *Geology*. <https://doi.org/10.1130/g24930a.1>
- Klinkenberg LJ (1941) The permeability of porous media to liquids and gases. *Drilling and Production Practice: American Petroleum Institute*: 200–213.
- Kramm U (1985) Sr-Isotopenuntersuchungen zur Genese der Strontianitlagerstätte Münsterland/Westfalen. *Fortschr Miner* 63:124
- Kummerow J (2006) The influence of intergranular, supercritical water on the elastic properties of rocks. Dissertation, Freie Universität Berlin
- La Bruna V, Lamarche J, Agosta F, Rustichelli A, Giuffrida A, Salardon R, Marié L (2020) Structural diagenesis of shallow platform carbonates: role of early embrittlement on fracture setting and distribution, case study of Monte Alpi (Southern Apennines, Italy). *J Struct Geol* 131:103940. <https://doi.org/10.1016/j.jsg.2019.103940>

- Lee EY, Kominz M, Reuning L, Gallagher S, Takayanagi H, Ishiwa T, Knierzinger W, Wagerich M (2021) Quantitative compaction trends of Miocene to Holocene carbonates off the west coast of Australia. *Aust J Earth Sci* 68:1149–1161. <https://doi.org/10.1080/08120099.2021.1915867>
- Leuthold J, Gerolymatou E, Vergara MR, Triantafyllidis T (2021) Effect of compaction banding on the hydraulic properties of porous rock: part I—experimental investigation. *Rock Mech Rock Eng* 54(6):2671–2683. <https://doi.org/10.1007/s00603-021-02427-w>
- Lowe DR, Guy M (2000) Slurry-flow deposits in the Britannia Formation (Lower Cretaceous), North Sea: a new perspective on the turbidity current and debris flow problem. *Sedimentology* 47(1):31–70. <https://doi.org/10.1046/j.1365-3091.2000.00276.x>
- Lucia FJ, Kerans C, Jennings JW Jr (2003) Carbonate reservoir characterization. *J Petrol Technol* 55(06):70–72. <https://doi.org/10.2118/82071-jpt>
- Machel HG, Grobe M (2001) Bacterial and thermochemical sulfate reduction in diagenetic settings—old and new insights. *Sed Geol* 140(1):143–175. [https://doi.org/10.1016/S0037-0738\(00\)00176-7](https://doi.org/10.1016/S0037-0738(00)00176-7)
- Masters BA, Scott RW (1979) Calcispheres and Nannoconids. *Paleontology. Encyclopedia of Earth Science*. Springer, Berlin, Heidelberg
- Mazur S, Scheck-Wenderoth M (2005) Constraints on the tectonic evolution of the Central European Basin System revealed by seismic reflection profiles from Northern Germany. *Neth J Geosci* 84(4):389–401. <https://doi.org/10.1017/S001677460002120X>
- Miller KG, Kominz MA, Browning JV, Wright JD, Mountain GS, Katz ME, Sugarman PJ, Cramer BS, Christie-Blick N, Pekar SF (2005) The Phanerozoic record of global sea-level change. *Science* 310(5752):1293–1298. <https://doi.org/10.1126/science.1116412>
- Miocic JM, Girard J-P, Schöner R, Gaupp R (2020) Mudstone/sandstone ratio control on carbonate cementation and reservoir quality in Upper Permian Rotliegend sandstones, offshore the Netherlands. *Mar Petrol Geol*. <https://doi.org/10.1016/j.marpetgeo.2020.104293>
- Mohrdieck P (1996) Ergebnisse geologisch-hydrogeologischer Untersuchungen bei der Herstellung eines Injektionssohle in Mergelgesteinen der Oberkreide. Dissertation, RWTH Aachen
- Monsees AC, Busch B, Schöner N, Hilgers C (2020) Rock typing of diagenetically induced heterogeneities: a case study from a deeply-buried clastic Rotliegend reservoir of the Northern German Basin. *Mar Petrol Geol* 113:104163. <https://doi.org/10.1016/j.marpetgeo.2019.104163>
- Monsees AC, Busch B, Hilgers C (2021) Compaction control on diagenesis and reservoir quality development in red bed sandstones: a case study of Permian Rotliegend sandstones. *Int J Earth Sci* 110(5):1683–1711. <https://doi.org/10.1007/s00531-021-02036-6>
- Morad S, Al Suwaidi M, Mansurbeg H, Morad D, Ceriani A, Paganoni M, Al-Aasm I (2019) Diagenesis of a limestone reservoir (Lower Cretaceous), Abu Dhabi, United Arab Emirates: comparison between the anticline crest and flanks. *Sed Geol* 380:127–142. <https://doi.org/10.1016/j.sedgeo.2018.12.004>
- Moshier SO (1989) Microporosity in micritic limestones: a review. *Sed Geol* 63(3):191–213. [https://doi.org/10.1016/0037-0738\(89\)90132-2](https://doi.org/10.1016/0037-0738(89)90132-2)
- Munnecke A, Wright VP, Nohl T (2023) The origins and transformation of carbonate mud during early marine burial diagenesis and the fate of aragonite: a stratigraphic sedimentological perspective. *Earth Sci Rev* 239:104366. <https://doi.org/10.1016/j.earscirev.2023.104366>
- Nadeau PH, Hurst A (1991) Application of back-scattered electron microscopy to the quantification of clay mineral microporosity in sandstones. *J Sediment Res* 61(6):921–925. <https://doi.org/10.1306/d4267807-2b26-11d7-8648000102c1865d>
- Odin G (1990) Clay mineral formation at the continent-ocean boundary: the verdine facies. *Clay Miner* 25(4):477–483. <https://doi.org/10.1180/claymin.1990.025.4.06>
- Paxton ST, Szabo JO, Ajdukiewicz JM, Klimentidis RE (2002) Construction of an intergranular volume compaction curve for evaluating and predicting compaction and porosity loss in Rigid-Grain sandstone reservoirs. *AAPG Bull* 86(12):2047–2067. <https://doi.org/10.1306/61eaddfa-173e-11d7-8645000102c1865d>
- Petrash DA, Bialik OM, Bontognali TRR, Vasconcelos C, Roberts JA, McKenzie JA, Konhauser KO (2017) Microbially catalyzed dolomite formation: from near-surface to burial. *Earth Sci Rev* 171:558–582. <https://doi.org/10.1016/j.earscirev.2017.06.015>
- Playà E, Travé A, Caja MA, Salas R, Martín-Martín JD (2010) Diagenesis of the Amposta offshore oil reservoir (Amposta Marino C2 well, Lower Cretaceous, Valencia Trough, Spain). *Geofluids* 10(3):314–333. <https://doi.org/10.1111/j.1468-8123.2009.00266.x>
- Prajapati N, Selzer M, Nestler B, Busch B, Hilgers C (2018) Modeling fracture cementation processes in calcite limestone: a phase-field study. *Geother Energy* 6:7. <https://doi.org/10.1186/s40517-018-0093-4>
- Püttmann T, Mutterlose J (2021) Paleoeology of late cretaceous coccolithophores: insights from the shallow-marine record. *Paleoceanogr Paleoclimatol*. <https://doi.org/10.1029/2020PA004161>
- Rashid F, Glover PWJ, Lorinczi P, Hussein D, Lawrence JA (2017) Microstructural controls on reservoir quality in tight oil carbonate reservoir rocks. *J Petrol Sci Eng* 156:814–826. <https://doi.org/10.1016/j.petrol.2017.06.056>
- Regnet JB, Robion P, David C, Fortin J, Brigaud B, Yven B (2015) Acoustic and reservoir properties of microporous carbonate rocks: Implication of micrite particle size and morphology. *J Geophys Res Solid Earth* 120(2):790–811. <https://doi.org/10.1002/2014jb011313>
- Reuning L, Reijmer J, Mattioli E (2006) Aragonite cycles: diagenesis caught in the act. *Sedimentology* 53:849–866. <https://doi.org/10.1111/j.1365-3091.2006.00799.x>
- Reuning L, Deik H, Petrick B, Auer G, Takayanagi H, Iryu Y, Courtillot M, Bassetti M-A (2022) Contrasting intensity of aragonite dissolution and dolomite cementation in glacial versus interglacial intervals of a subtropical carbonate succession. *Sedimentology* 69(5):2131–2150. <https://doi.org/10.1111/sed.12985>
- Rider M, Kennedy M (2011) The geological interpretation of well logs. Rider-French Consulting Ltd., Scotland, pp 165–168
- Rieckmann M (1970) Untersuchung von Turbulenzerscheinungen beim Fließen von Gasen durch Speichergesteine unter Berücksichtigung der Gleitströmung. *Erdöl-Erdgas-Zeitschrift*, Heft 2(86):36–51
- Rudolph T, Melchers C, Minke A, Coldewey WG (2010) Gas seepages in Germany: revisited subsurface permeabilities in the German mining district. *AAPG Bull* 94(6):847–867. <https://doi.org/10.1306/10210909074>
- Ryan PC, Hillier S (2002) Berthierine/chamosite, corrensite, and discrete chlorite from evolved verdine and evaporite-associated facies in the Jurassic Sundance Formation. *Wyom Am Mineral* 87(11–12):1607–1615. <https://doi.org/10.2138/am-2002-11-1210>
- Scheck-Wenderoth M, Krzywiec P, Zühlke R, Maystrenko Y, Froitzheim N (2008) Permian to Cretaceous tectonics. In: McCann T (ed) *The Geology of Central Europe Volume 2: Mesozoic and Cenozoic*, 2nd edn. Geological Society Publishing House, London, pp 999–1030

- Schmidt C, Busch B, Hilgers C (2021) Lateral variations of detrital, authigenic and petrophysical properties in an outcrop analog of the fluvial Plattensandstein, Lower Triassic, Central S-Germany. *Zeitschrift der Deutschen Gesellschaft für Geowissenschaften* 172. Heft 4:541–564. <https://doi.org/10.1127/zdgg/2020/0234>
- Shinn EA, Halley RB, Hudson JH, Lidz BH (1977) Limestone compaction: an enigma. *Geology* 5(1):21–24. [https://doi.org/10.1130/0091-7613\(1977\)5%3c21:Lcae%3e2.0.Co;2](https://doi.org/10.1130/0091-7613(1977)5%3c21:Lcae%3e2.0.Co;2)
- Smodej J, Reuning L, Becker S, Kukla P (2019) Micro- and nanopores in intrasalt, microbialite-dominated carbonate reservoirs, Ara Group, South-Oman salt basin. *Mar Pet Geol* 104:389–403. <https://doi.org/10.1016/j.marpetgeo.2019.03.036>
- Stanchits S, Fortin J, Gueguen Y, Dresen G (2009) Initiation and propagation of compaction bands in dry and wet bentheim sandstone. *Pure Appl Geophys* 166:843–868. <https://doi.org/10.1007/s00024-009-0478-1>
- STD (2016) Stratigraphische Tabelle von Deutschland 2016. Deutsche Stratigraphische Kommission, Hrsg.; Redaktion, Koordination und Gestaltung: Menning, M Hendrich, A - Potsdam (GeoForschungsZentrum).
- Toffolo MB, Ricci G, Caneve L, Kaplan-Ashiri I (2019) Luminescence reveals variations in local structural order of calcium carbonate polymorphs formed by different mechanisms. *Sci Rep* 9(1):16170. <https://doi.org/10.1038/s41598-019-52587-7>
- Uffmann AK (2014) Paleozoic petroleum systems of northern Germany and adjacent areas: A 3D modeling study. Aachen, Techn. Hochsch.
- Vejbæk OV, Andersen C, Dusaar M, Herengreen GFW, Krabbe H, Leszczyński K, Lott GK, Mutterlose J, Van der Molen AS (2010) Cretaceous. In: Doornenbal JC, Stevenson AG (eds) *Petroleum Geological Atlas of the Southern Permian Basin Area* edn. EAGE Publications b.v, Houten, Netherlands, pp 195–209
- Versteegh GJM, Servais T, Streng M, Munnecke A, Vachard D (2009) A discussion and proposal concerning the use of the term calcispheres. *Palaeontology* 52(2):343–348. <https://doi.org/10.1111/j.1475-4983.2009.00854.x>
- Vodrazkova S, Munnecke A (2010) Calcispheres as a source of lime mud and peloids evidence from the early Middle Devonian of the Prague Basin, the Czech Republic. *Bull Geosci* 85:585–602. <https://doi.org/10.3140/bull.geosci.1206>
- Voigt E, Häntzschel W (1964) Gradierte Schichtung in der Oberkreide Westfalens. *Fortschr Geol Rheinland Westfalen* 7:495–548
- Voigt T, Kley J, Voigt S (2021) Dawn and dusk of Late Cretaceous basin inversion in central Europe. *Solid Earth* 12(6):1443–1471. <https://doi.org/10.5194/se-12-1443-2021>
- Volery C, Davaud E, Durlot C, Clavel B, Charollais J, Caline B (2010) Microporous and tight limestones in the Urgonian Formation (late Hauterivian to early Aptian) of the French Jura Mountains: Focus on the factors controlling the formation of microporous facies. *Sed Geol* 230(1–2):21–34. <https://doi.org/10.1016/j.sedgeo.2010.06.017>
- Weger RJ, Eberli GP, Baechle GT, Massaferro JL, Sun Y-F (2009) Quantification of pore structure and its effect on sonic velocity and permeability in carbonates. *AAPG Bull* 93(10):1297–1317. <https://doi.org/10.1306/05270909001>
- Wendler JE, Bown P (2013) Exceptionally well-preserved Cretaceous microfossils reveal new biomineralization styles. *Nat Commun* 4(1):2052. <https://doi.org/10.1038/ncomms3052>
- Wendler J, Willems H (2004) Pithonelloid wall-type of the Late Cretaceous calcareous dinoflagellate cyst genus *Tetratropis*. *Rev Palaeobot Palynol* 129(3):133–140. <https://doi.org/10.1016/j.revpalbo.2003.12.011>
- Westphal H, Munnecke A (1997) Mechanical compaction versus early cementation in fine-grained limestones: differentiation by the preservation of organic microfossils. *Sed Geol* 112(1):33–42. [https://doi.org/10.1016/S0037-0738\(97\)00033-X](https://doi.org/10.1016/S0037-0738(97)00033-X)
- Wiese F, Wood C, Kaplan U (2004) 20 years of event stratigraphy in NW Germany: advances and open questions. *Acta Geol Pol* 54:639–656
- Wilmens M, Dölling B, Hiss M, Niebuhr B (2019) The lower Upper Cretaceous of the south-eastern Münsterland Cretaceous Basin, Germany: facies, integrated stratigraphy and inter-basinal correlation. *Facies*. <https://doi.org/10.1007/s10347-018-0552-1>
- Wilson JL (1975) Carbonate facies in geologic history. Springer, New York
- Wirges J, Dodenhoff P (2019) Visualizing spatio-temporal data as an animation vs. as static maps: black coal mine shafts in the Ruhr region. <https://www.dataviz-jwirges.de/visualizing-spatio-temporal-data-as-an-animation-vs-as-static-maps/>. Accessed 20. January 2024
- Wolf KH (1965) Gradational sedimentary products of calcareous algae. *Sedimentology* 5(1):1–37. <https://doi.org/10.1111/j.1365-3091.1965.tb01556.x>
- Wolf EO (1995) Sedimentologie, Paläogeographie und Faziesentwicklung der Allochthonite des Campan von Beckum/Zentrales Münsterland. *Berliner Geowiss Abh* E16:305–333
- Worden R, Armitage P, Butcher A, Churchill J, Csoma A, Hollis C, Lander R, Omma J (2018) Petroleum reservoir quality prediction: overview and contrasting approaches from sandstone and carbonate communities. *Geol Soc Lond Spec Publ* 435:1–31. <https://doi.org/10.1144/SP435.21>
- Wulff L, Kaplan U, Mutterlose J (2017) Zur spätcretazischen Hebungsgeschichte des Raumes Halle (Westfalen): die Biostratigraphie der Rutschmassen des Hesselts. *Geologie Und Palaeontologie in Westfalen* 2017:5–19
- Wyrick GG, Borchers JW (1981) Hydrologic Effects of Stress-relief Fracturing in an Appalachian Valley. U.S. Government Printing Office, 12–13. <https://doi.org/10.3133/wsp2177>
- Xi K, Yingchang C, Jahren J, Zhu R, Bjørlykke K, Haile B, Lijing Z, Hellevang H (2015) Diagenesis and reservoir quality of the Lower Cretaceous Quantou Formation tight sandstones in the southern Songliao Basin, China. *Sed Geol* 330:90–107. <https://doi.org/10.1016/j.sedgeo.2015.10.007>
- Zhang S, Lu P (2019) Effect of micrite content on calcite cementation in an Upper Jurassic carbonate reservoir, Eastern Saudi Arabia. *J Pet Geol* 42(1):79–89. <https://doi.org/10.1111/jpg.12725>